Integrated transcriptomic profiling reveals a STING-mediated Type II Interferon signature in SOD1-mutant amyotrophic lateral sclerosis models

Check for updates

Jen Young Hiew[1], Yi Shan Lim[1], Huitao Liu[2] & Chen Seng Ng [1]✉

Inflammation is a hallmark of amyotrophic lateral sclerosis (ALS), particularly in cases with SOD1 mutations. Using integrative transcriptomics, we analyzed gene expression changes in mouse models throughout progression, human induced-pluripotent stem cells (hiPSCs), and post-mortem spinal cord tissue from ALS patients. We identified a conserved upregulation of interferon (IFN) genes and IFN-stimulating genes (ISGs) in both mouse models and human ALS, with a predominance Type I IFNs (IFN-α/β) in mice and Type II IFNs (IFN-γ) in humans. In mouse models, we observed robust and sustained upregulation of Type I and II ISGs, including ATF3, beginning at disease onset stage and persisting throughout disease progression. Single-cell transcriptomics further pinpointed vascular endothelial cells as a major source of ISGs. Furthermore, we found that the STING-TBK1 axis is essential for the induction of Type II ISGs in ALS, as its deletion impaired their expression. Our study uncovers a conserved ISGs signature across ALS models and patients, highlighting the potential role of innate immune activation in ALS pathogenesis. These findings suggest that ISGs may serve as potential biomarkers and therapeutic targets for ALS.

Amyotrophic lateral sclerosis (ALS), also known as Lou Gehrig's disease, is a fatal neurodegenerative disorder characterized by progressive degeneration of both upper and lower motor neurons, culminating in muscle atrophy, paralysis, and eventually respiratory failure. ALS typically affects individuals between 40 to 60 years of age, with a median survival of three to five years post-diagnosis[1]. While approximately 10% of ALS cases are familial (fALS), linked to inherited genetic mutations, the majority (90%) are sporadic (sALS) with no clear genetic etiology[2].

The most common genetic cause of ALS in individuals of European ancestry is a hexanucleotide repeat expansion (HRE) in the C9orf72 gene, responsible for 40% to 60% of fALS cases and 5% to 10% of sALS cases[3]. C9orf72-associated ALS (C9orf72-ALS) often presents with frontotemporal dementia, marked by bulbar onset and cognitive-behavioral deficits. Mutations in SOD1 gene represent the second most common genetic driver, implicated in 12% to 24% of fALS and 1% of sALS[4]. Other mutations in genes such as TAR DNA-binding protein 43 (TDP-43) and fused in sarcoma (FUS) collectively contribute to another 1% to 5% of fALS cases, highlighting the complex genetic landscape of ALS[5,6]. Although the specific

triggers of ALS remain largely unknown, increasing evidence suggests that dysfunctional inflammatory signaling plays a critical role[7], offering a valuable target for research and potential therapeutic strategies.

Neuroinflammation is increasingly recognized as a hallmark of ALS pathology, primarily driven by chronic activation of glial cells, especially microglia [the resident immune cells of the central nervous system (CNS)] and astrocytes, which exhibit dual neuroprotective and neurotoxic roles[7–12]. While the precise mechanisms driving inflammation in ALS remain incompletely understood, several critical pathways have been implicated. Activated glial cells release pro-inflammatory cytokines such as tumor necrosis factor-alpha (TNF-α) and interleukin-1β (IL-1β), directly inducing neuronal apoptosis[7,8,13], while also contributing to oxidative stress through the generation of reactive oxygen and nitrogen species. Peripheral immune cells, including monocytes and lymphocytes, further infiltrate the CNS, amplifying neuroinflammation and accelerating neurodegeneration. Recent studies have highlighted the pivotal role of the cGAS-STING pathway in linking molecular aberrations to inflammatory cascades across various ALS models. Pathogenic aggregates of SOD1 and TDP-43 disrupt mitochondrial

[1]School of Science, Monash University Malaysia, Jalan Lagoon Selatan, 47500 Selangor, Malaysia. [2]School of Biological Engineering, College of Advanced Interdisciplinary Science and Technology, Henan University of Technology, 100 Lianhua Street, Zhongyuan District, Zhengzhou, 450001, China. ✉e-mail: ng.chenseng@monash.edu

Article

integrity, releasing mitochondrial DNA and RNA hybrids that activate the cGAS/DDX41-STING signaling. This triggers type I interferon (IFN-I) production and ISGs expression, intensifying neuronal damage and disease progression[14,15].

In C9orf72-ALS, loss of C9orf72 function impairs lysosomal degradation of STING in myeloid cells (e.g. macrophages), leading to persistent immune activation and systemic inflammation[16]. However, while C9orf72 deficiency in murine models recapitulates immune dysregulation, it fails to induce neurodegeneration, suggesting cell-type-specific contributions[16]. Contrastingly, neuron-intrinsic STING activation has been proposed as a key driver of neuroinflammation and degeneration in ALS[17]. Using both in vitro hiPSC-derived neurons and in vivo models, their findings implicate neuron-intrinsic STING signaling in disease progression. These divergent findings underscore the multifactorial nature of ALS pathogenesis, wherein both neuron-intrinsic and extrinsic mechanisms may synergize to drive disease progression in a context-dependent manner. Critically, both paradigms converge on STING signaling as a central pathogenic node, highlighting its therapeutic potential[16,17]. Indeed, STING inhibition alleviates neuropathology and improves motor function in *SOD1* and *TDP-43* mutant models[14,15], reinforcing the cGAS-STING axis as a crucial link between molecular aberrations and neuroinflammation in ALS.

Integrative analysis of multi-omics datasets offers a powerful strategy to uncover common pathological features and potential therapeutic targets. Genome-wide association studies and transcriptomic profiling have revealed numerous candidate genes and dysregulated pathways implicated in ALS, offering insights into disease mechanisms and biomarkers. Despite the inherent heterogeneity of ALS, integration of data from both murine and human models can highlight shared gene expression patterns that may be obscured in isolated studies. Reanalysis of existing datasets offers an additional dimension for discovering insights beyond the scope of the original research. Leveraging this approach, we harmonized RNA-sequencing data from murine models with human iPSC-derived cells and post-mortem tissues to resolve conserve and species-specific pathways. We identified sustained IFN-I, IFN-II, and ISGs induction from disease onset to end-stage across models, with vascular endothelial cells emerging as unexpected key contributors to these signatures. Strikingly, human ALS tissues exhibited predominant IFN-II and its associated ISGs activation, contrasting with murine models dominated by IFN-I signatures. These work advances our understanding of ALS pathophysiology and identifies conserved nodes for diagnostic or therapeutic innovation.

Results
Distinct temporal expression dynamics in ALS model
Our database search strategy identified two bulk-RNA-seq datasets with time-course designs for ALS (Fig. 1a). The first dataset (Maniatis S. et al.[18]) utilizes quantitative spatial transcriptomics to profile gene expression in lumbar spinal cord tissue sections (L3-L5) from SOD1-G93A mice at pre-symptomatic [postnatal day 30 (P30)], onset (P70), symptomatic (P100), and end-stage (P120) time-points[18]. This data was generated using the 10X Genomics platform, capturing polyadenylated RNA on arrays of spatially barcoded DNA capture probe. The second study (Phatnani H. et al.[19]) involves a longitudinal series of whole spinal-cord samples from adult pre- and post-symptomatic ALS mice[19]. In this investigation, RNA isolated from the whole spinal cord tissue specimens underwent high-throughput next-generation-based transcriptomics multiplexing to assess gene expression patterns (Fig. 1a). We prioritized the dataset from Phatnani et al.[19] for subsequent analysis due to its advantages in using the whole spinal cord organ. This approach: (1) captures the heterogeneity of ALS progression and the diverse gene expression and pathology across different spinal cord segments; (2) allows for broader investigation of ALS-related effects in non-motor neuron cells; (3) increases the potential to identify biomarkers from various regions; and (4) enhances clinical relevance by reflecting the widespread degeneration characteristic of ALS. Additionally, Phatnani et al.[19] employed the widely used and standardized Illumina platform, facilitating comparability with subsequent studies. All samples underwent
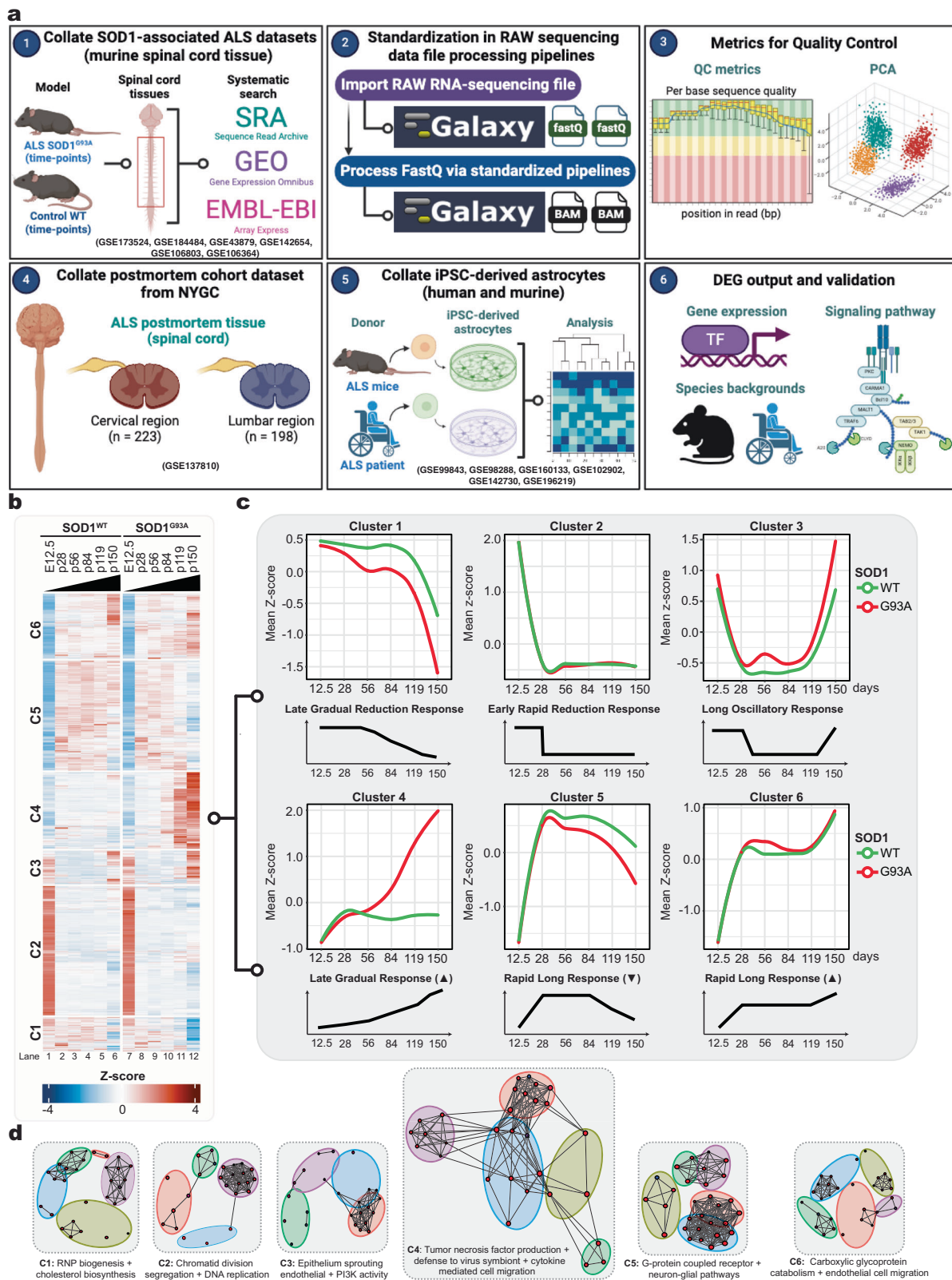
rigorous quality control, and principal component analysis was employed to assess the effects of sequencing and batch-related confounding variables. For this study, we included six datasets from mouse SOD1-associated ALS models, as well as ALS iPSCs carrying SOD1, VCP, C9orf72, and FUS mutations. Additionally, spinal cord tissues from patients with sALS (lacking identifiable ALS mutations) were also included (Table 1).

To elucidate the common underlying mechanisms driving the dynamics and progression of SOD1-mediated ALS, we initially focused on identifying gene expression changes. We characterized cellular systems with temporal precision across six distinct time points [embryonic day 12.5 (E12.5), P28, P56 (pre-symptomatic); P84 (onset); P119 and P150 (symptomatic)]. Unsupervised clustering of significantly dysregulated genes ($p < 0.05$) revealed a series of distinct response patterns shared across genotypes and time courses. Using k-means clustering, we pre-set the number of clusters (k) to test multiple values and identified six primary gene clusters (Fig. 1b) based on the most uniform and distinct separation of gene expression profiles. Each cluster demonstrated unique dynamic alterations in gene expression preferences. Cluster 1 manifested a progressive, gradual decline in expression ("*late gradual reduction*" response) associated with cholesterol biosynthetic process, including genes such as *LSS, TM7SF2, HMGCS1, CYP51*, and *FDPS* ($p = 3.08 \times 10^{-6}$). This cluster also included genes involved in translation and ribosomal protein synthesis machinery, such as *MRPL21, EIF5B, RPL12*, and *FAU* ($p = 5.72 \times 10^{-6}$; Fig. 1c, d). Cluster 2 showed an immediate, rapid reduction in genes associated with cell cycle and DNA replication, evident as early as P28 ("*early rapid reduction*" response), featuring genes like *MCM4, TOP2A, HFM1, PCNA*, and *DNA2* ($p = 1.81 \times 10^{-23}$). Additionally, it contained transcription factors linked to cell fate and development, such as *HDAC1, HOXC10 OLIG3, SOX6*, and *GLI3* ($p = 2.15 \times 10^{-25}$; Fig. 1c, d). Notably, Cluster 3 displayed oscillatory expression dynamics in genes primarily involved in sprouting angiogenesis, including *VEGFA, SH2B3, THBS1, ADAM8*, and *ITGB1* ($p = 2.82 \times 10^{-14}$; Fig. 1c, d). Cluster 4 was characterized by a late but progressive upregulation of cytokines and inflammatory molecules (*CXCL9, CXCL10, CCL2, CCL5, ITGAX, AXL, CLEC7a; p = 1.67 \times 10^{-21}$), corroborating previous findings of pre-symptomatic upregulation of *TYROBP, APOE*, and *TREM2* in G93A model[18,20]. Furthermore, we observed similar disease-stage upregulation patterns for *LPL, B2M*, and *CX3CR1*, which function under the TREM2-TYROBP pathway (Fig. 1c, d)[21,22].

Multiple genes enriched in the early peaking classes ["*rapid long responses (increase/decrease)*"] demonstrated contrasting dynamics within Cluster 5 and 6. Cluster 5 showed a rapid, progressive loss of genes linked to G-protein coupled receptor and neuron-glial signaling pathways (*GABBR1, ADRA1A, PENK, OPRK1, OPRM1; p = 9.86 \times 10^{-11}$). At the molecular function level, this cluster also displayed a pronounced, gradual loss of genes regulating myelin sheath formation and voltage-gated membrane potential (*KCNJ3, SCN1A, GPM6B*, and *MAL; p = 3.33 \times 10^{-21}$ (Fig. 1c, d). Conversely, Cluster 6 demonstrated a rapid, progressive increase in gene expression, including genes implicated in carboxylic acid catabolic process, such as *CRYL1, ACADL, LDHD*, and *NUDT19* ($p = 3.18 \times 10^{-15}$; Fig. 1c, d). Across all response classes, Cluster 1 and 5 demonstrated decreased expression in G93A compared to WT controls, while changes in Cluster 2, 3 and 6 were less pronounced. Importantly, most genes dynamically changing in Cluster 4 showed the most significant upregulation in G93A compared to WT over time (Fig. 1c). Notably, cytokines and pro-inflammatory genes in this cluster showed a marked increase throughout ALS disease progression without reaching a plateau by the study's endpoint. In summary, our re-analysis of time-series expression studies to construct dynamics networks identified differentially expressed genes (DEGs) involved in multiple biological processes at distinct phases of the disease.

Highly inflammatory and ISGs immune signature at ALS onset stage
To elucidate the relationship between gene expression changes and ALS disease progression, we conducted a time-course transcriptomic analysis in the G93A SOD1 mutant mouse model. Time points were selected to capture

a

1. **Collate SOD1-associated ALS datasets (murine spinal cord tissue)**
Model — Spinal cord tissues — Systematic search
ALS SOD1^G93A (time-points)
Control WT (time-points)
SRA — Sequence Read Archive
GEO — Gene Expression Omnibus
EMBL-EBI — Array Express
(GSE173524, GSE184484, GSE43879, GSE142654, GSE106803, GSE106364)

2. **Standardization in RAW sequencing data file processing pipelines**
Import RAW RNA-sequencing file — Galaxy fastQ fastQ
Process FastQ via standardized pipelines — Galaxy BAM BAM

3. **Metrics for Quality Control**
QC metrics — Per base sequence quality — position in read (bp)
PCA

4. **Collate postmortem cohort dataset from NYGC**
ALS postmortem tissue (spinal cord)
Cervical region (n = 223) — Lumbar region (n = 198)
(GSE137810)

5. **Collate iPSC-derived astrocytes (human and murine)**
Donor — iPSC-derived astrocytes — Analysis
ALS mice
ALS patient
(GSE99843, GSE98288, GSE160133, GSE102902, GSE142730, GSE196219)

6. **DEG output and validation**
Gene expression — TF
Signaling pathway
Species backgrounds

b

SOD1^WT SOD1^G93A
E12.5 p28 p56 p84 p119 p150 E12.5 p28 p56 p84 p119 p150
C6, C5, C4, C3, C2, C1
Lane 1 2 3 4 5 6 7 8 9 10 11 12
Z-score: -4 0 4

c

Cluster 1 — Late Gradual Reduction Response
Cluster 2 — Early Rapid Reduction Response
Cluster 3 — Long Oscillatory Response
Cluster 4 — Late Gradual Response (▲)
Cluster 5 — Rapid Long Response (▼)
Cluster 6 — Rapid Long Response (▲)

SOD1: WT, G93A

d

C1: RNP biogenesis + cholesterol biosynthesis
C2: Chromatid division segregation + DNA replication
C3: Epithelium sprouting endothelial + PI3K activity
C4: Tumor necrosis factor production + defense to virus symbiont + cytokine mediated cell migration
C5: G-protein coupled receptor + neuron-glial pathways
C6: Carboxylic glycoprotein catabolism + endothelial cell migration

the full spectrum of disease development: from pre-onset stages (embryonic and adult) through onset and symptomatic phases to the terminal stage. Initial analysis of the entire transcriptome at E12.5 revealed no significant differences between G93A compared to WT mice (FDR < 0.05; Supplementary Fig. 1a). This is consistent with the absence of an overt phenotype at this stage. However, modest gene expression changes emerged by weaning

age (P28), with eight DEGs identified in SOD1 mutant mice (adjusted $P < 0.05$): three upregulated and five downregulated (Fig. 2a). At the asymptomatic P56 stage, the ALS model displayed a substantial increase in DEGs, with a total of 122 genes: 93 upregulated and 29 downregulated (Fig. 2b, *left*). Upregulated genes included stress-induced transcription components *KLF2, CEBPB, ATF3, TCIM*. Functional enrichment analysis

Fig. 1 | Temporal transcriptomic analysis identifies persistent activation of cytokines during disease progression in ALS. a Schematic representation of analytical workflow. Integrated analysis of RNA-seq data arising from multiple published studies, located through an extensive computerized search using specific key-terms reported in peer-review journals. The data was uniformly processed via Galaxy web-based platform before further subjecting to more downstream analysis. **b** *K*-means clustering of significantly affected genes identifies 6-coordinated expression modules as determined by RNA-seq in bulk from WT and SOD1-G93A mice. Vertical lane: mean of biological replicates of whole spinal cord tissue cells from WT versus SOD1-G93A (n ≥ 3 mice/age group, mean Z-scores based on Log-transformed CPM). **c** (Upper section) Z-score mean

expression across time courses for age of WT and SOD1-G93A mice ranging from embryonic day 12.5 to postnatal day 150; (*Lower section*) Simplified expression dynamics patterns for G93A, modeled to illustrate the general trend observed within each cluster (not directly generated from the expression data). The y-axis shows the average Z-score; the *x*-axis indicates the age of mice postnatal. **d** The primary biological processes or pathways enriched within these six-modules are examined in their temporal context while comparing across genotypes. Each individual cluster contains interconnected nodes, representing individual genes, with edges indicating functional relationships between them.

Table 1 | Datasets included in the integrated analysis

Reference	Accession #	Mutation	Samples (n)	Platform	Library type	Layout	Organism	Sequencing type	Sample type
Phatnani et al.[19]	GSE43879	SOD1	16	Illumina	poly(A)	Single	Mus musculus (C57BL/6J)	Bulk	Whole spinal cord
Herskovits et al.[100]	GSE106803	SOD1	6	Illumina	poly(A)	Single	Mus musculus (C57BL/6J)	Bulk	Whole spinal cord
Fernández-Beltrán et al.[39]; Fernández-Beltrán et al.[101]	GSE184484	SOD1	10	Illumina	poly(A)	Paired	Mus musculus (C57BL/6J)	Bulk	Spinal cord (L)
Henriques et al. 2017	GSE106364	SOD1	10	Illumina	poly(A)	Single	Mus musculus (C57BL/6J)	Bulk	Spinal cord (L)
MacLean et al.[47]	GSE173524	SOD1	12	Illumina	poly(A)	Paired	Mus musculus (C57BL/6J)	Single-cell	Spinal cord (L)
Luisier et al.[102]; Hall et al.[57]	GSE99843	VCP	4	Illumina	poly(A)	Single	Homo sapiens	Bulk	iPSCs
	GSE98288	VCP	6	Illumina	poly(A)	Single	Homo sapiens	Bulk	iPSCs
	GSE160133	VCP	9	Illumina	poly(A)	Paired	Homo sapiens	Bulk	iPSCs
Tyzack et al.[55]	GSE102902	SOD1	3	Illumina	poly(A)	Single	Homo sapiens	Bulk	iPSCs
Birger et al.[56]	GSE142730	C9ORF72	4	Illumina	poly(A)	Single	Homo sapiens	Bulk	iPSCs
Stoklund et al.[58]	GSE196219	FUS	12	Illumina	poly(A)	Single	Homo sapiens	Bulk	iPSCs
NYGC ALS Consortium	GSE137810	Sporadic	(C) 275 / (L) 255	Illumina	poly(A)	Paired	Homo sapiens	Bulk	Postmortem spinal cord tissues

C Cervical region, *L* Lumbar region

of these genes in G93A revealed an overpresentation of processes related to the negative regulation of cytokine production (e.g. *ZFP36, THBS1, SRGN, LRRC32*), epithelial cell differentiation, blood vessel endothelial cell migration (*APOLD1, ACVRL1*), regulation of hemopoiesis (e.g. *ADA, ZBTB1, PGLYRP1, RBP1*), and circadian rhythm dysfunction (e.g. *DBP, CIART, ADAMTS1, ID1*) – a process previously implicated in ALS pathophysiology (Fig. 2c, *left*)[23,24]. Conversely, downregulated genes in G93A at P56 were enriched in calcium and secondary messenger mediated signaling (e.g. *ERBB3, OPRM1, CASQ1, CCRL2*) (Fig. 2c, *right*). Nearing disease onset (P84), the number of DEGs escalated further to a total of 331, with 315 upregulated and 16 downregulated genes (Fig. 2b, *right*). These observations suggest that gene expression alterations occur as early as the weaning stage and become progressively more pronounced throughout disease progression in the SOD1-linked ALS model.

To pinpoint mechanisms driving disease onset, we analyzed genes differentially expressed at P84. This time point corresponds to the emergence of disease symptoms in SOD1 G93A, G86R and G37R mice[25,26]. Key histopathological features at this stage include early astrogliosis and microgliosis, axonal transport deficits, mitochondrial dysfunction, and aberrant neurofilament processing, culminating in motor neuron loss, muscle atrophy, and the onset of paralysis[27–29]. Our analysis identified that the majority of the downregulated genes at P84 are associated with Notch and P38 MAPK signaling pathways (e.g. *DLK2*), implicated in calcium ion binding and protein heterodimerization dysfunction. Moreover, we found downregulation of genes involved in mitochondrial dysfunction (e.g. *LYRM7*), neuron development, and cerebrospinal fluid (CSF) regulation (e.g. *CAR4, CCDC122*). These

findings support the initiation of neuromuscular deterioration at this stage, consistent with the appearance of paralysis in the G93A model. Conversely, Circos plot network analysis of upregulated genes at P84 presented a notable enrichment of genes associated with biological processes such as "*regulation of innate immune response*", and "*defense response to virus*". Notably, components of the interferon-alpha/beta receptor pathway (e.g. *IFITM3, GBP7, ZC3HAV1, IFIH1, APOBEC1, ISG15, IRF7, OAS3, OASL, IFIT1, MX1*) were among the upregulated signatures (Fig. 2d, Supplementary Fig. 1b). Molecular functional analysis reinforced these findings, demonstrating a significant enrichment in chemokine activity, STAT family protein binding, as well as immune-receptor binding among the upregulated cluster (Supplementary Fig. 1b). This strongly suggests the activation of inflammatory and interferon-associated antiviral responses in G93A at P84.

IFNs are potent cytokines that regulate inflammation and immune responses, classified into three types: type I (IFN-I, primarily IFN-α/β), type II (IFN-II, IFN-γ), and type III (IFN-III, IFN-λ). IFN-I and IFN-III signal through distinct receptors (IFNAR1/2 and IFNLR1/IL10R2, respectively), activating Janus kinases (JAK)-signal transducer and activator of transcription (STAT) signaling, which forms the IFN-stimulated gene factor 3 (ISGF3) complex [STAT1, STAT2, and interferon regulatory factor 9 (IRF9)] to induce the expression of ISGs. IFN-II, on the other hand, signals through IFNGR1/2, inducing STAT1 homodimerization that also drive ISGs expression[30]. We next inferred the classification of ISGs from their characterized regulon expression within the INTERFEROME database[31,32]. This database integrates ISGs identified through high-throughput and perturbations experiments across various species. This allows for robust
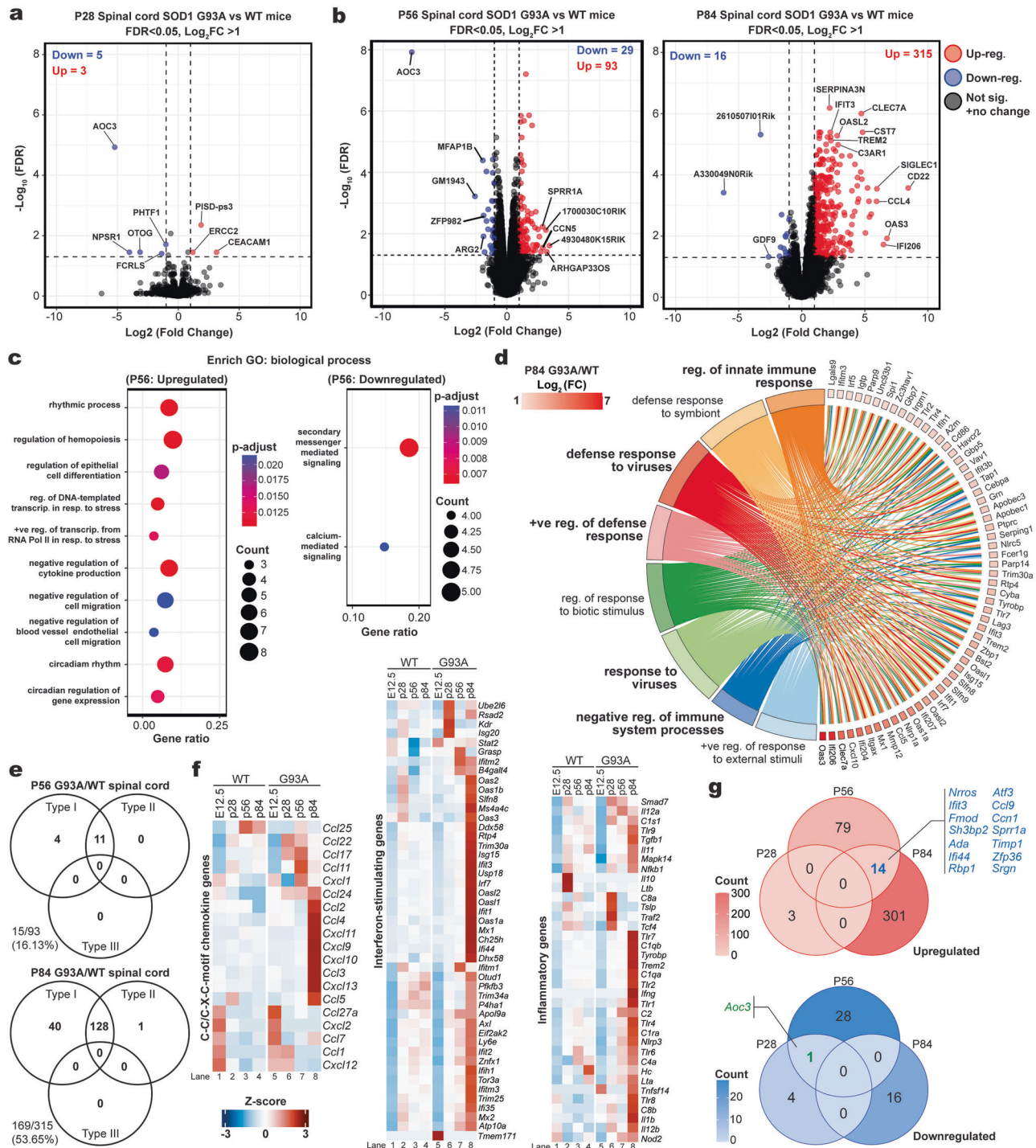
Fig. 2 | Induction of Type I and II ISGs during pre-symptomatic stage preceding the onset of ALS development. Volcano plots of normalized differentially expressed genes from whole spinal cord of G93A over WT mice at postnatal day 28 (**a**), day 56 or 84 (**b**). Genes upregulated and downregulated (*Dotted lines*: Log2 = 1/-1, 2-fold expression changes) are shown in red and blue, respectively. In this plot, the -Log$_{10}$ FDR value of each gene is plotted (on the vertical axis) against its log 2-fold change (on the horizontal axis). **c** Enrichment pathway analysis of Biological Process (BP) GO terms of up- and down-regulated DEGs in G93A/WT postnatal day 56 mice. Analysis was performed using a hypergeometric overrepresentation test against the GO database, with significance achieved at Q-value < 0.05. Dots represent term enrichment, *p*-values indicating the statistical significance of the enrichment are represented along a gradient color from blue (less significant) to red (most significant). The sizes of the dots represent the count of DEGs

belonging to each term. **d** The circos plot illustrating the functional characterization of genes expression modules in G93A/WT postnatal day 84 mice. Each segment ring in the right side represents a module of co-expressed genes identified from upregulated DEGs between G93A and WT mice. The left segmented ring displays enriched GO terms that characterize these modules. Each line represents a pairwise dataset overlap as determined by GSEA analysis and filtered by *p* < 0.05. **e** The Venn diagram illustrates the classification of up-regulated DEGs from G93A/WT at both P56 and P84 mice into categories of Type I, II, and/or III ISGs. **f** Heatmap of selected chemokines, pro-inflammatory, and interferon-stimulating genes in G93A versus WT mice ranging from embryonic day 12.5 to postnatal day 84. **g** Venn diagram illustrates the genes that overlap across the pre-symptomatic stage of G93A/WT mice, from P28 to P84.

cross-species identification and classification of ISGs signatures. Remarkably, the proportion of ISGs among upregulated genes in G93A mice increased substantially with disease progression. At P56, during the asymptomatic stage, only 16.12% (15 of 93 genes, $P_{Fisher} = 6.39 \times 10^{-5}$) of upregulated genes were classified as ISGs. Of these, the majority (11 of 15) were regulated by both IFN-I and IFN-II (Fig. 2e, *upper*). By P84, corresponding to disease onset, the proportion of ISGs among upregulated genes surged to 53.7% (169 of 315 genes, $P_{Fisher} = 2.23 \times 10^{-55}$) (Fig. 2e, *lower*). This amplified ISGs signature was predominantly driven by IFN-I and IFN-II, with 75.73% (128/169) of ISGs co-regulated by both pathways. A smaller subset (23.67%, 40/169) were specifically regulated by IFN-I, while minimal contributions from IFN-II (0.59%, 1/169) were observed (Fig. 2e, *lower*). Notably, no genes were found to be exclusively regulated by IFN-III at either time point (Fig. 2e).

Further comparative analysis revealed a pronounced activation of (1) inflammatory responses—IFN-γ (mean FC = 3.59), *TREM2* (mean FC = 4.95), interleukin [*IL12* (mean FC = 3.21), *IL1B* (mean FC = 3.94)], and NF-κB signaling [e.g. *NFKB1* (mean FC = 2.67), *TNFRSF1A* (mean FC = 3.65)] (Fig. 2f, *right*); (2) chemokines—IFN-inducible chemokines RANTES/*CCL5* (mean FC = 13), MCP-1/*CCL2* (mean FC = 45.25), MIP-1α/CCL3 (mean FC = 15.78), MIP-1β/*CCL4* (mean FC = 60.96), *CCL12* (mean FC = 18.64), and IP-10/*CXCL10* (mean FC = 21.56) (Fig. 2f, *left*), and (3) ISGs responses, which were evidenced by pronounced increases in genes such as *OAS3* (mean FC = 108.38), CD169/*SIGLEC1* (mean FC = 62.25), *IFI206* (mean FC = 89.26), *IFI44* (mean FC = 27.1), *IFI204* (mean FC = 21.26), *CH25H* (mean FC = 21.4), *MX1* (mean FC = 15.76), *SERPINF2* (mean FC = 13.93), *USP18* (mean FC = 7.21), *OASL2* (mean FC = 7.01), *IRF7* (mean FC = 7.01), *IFIT1* (mean FC = 6.36), *ISG15* (mean FC = 5.39), *C1QB* (mean FC = 4.82), *GBP3* (mean FC = 3.71), MDA5/*IFIH1* (mean FC = 2.68), *IFITM3* (mean FC = 2.16), and RIG-I/*DDX58* (mean FC = 2.91), which were among the top upregulated genes affected and were highly increased in the spinal cord at P84 (Fig. 2f, *middle*). These observations further reaffirmed our previous findings of robust ISGs induction in SOD1 mutant ALS models[14].

To investigate whether the observed phenomena is specific to the G93A mutation, we extended our analysis to another well-established ALS-linked SOD1 mutation, G86R[33]. At disease onset (P95), we identified 312 DEGs (FDR < 0.05), with 302 upregulated and 10 downregulated genes (Supplementary Fig. 2a). Mirroring the G93A model, GO analysis of G86R upregulated genes revealed significant enrichment in pathways related to cytokine-mediated signaling and regulation of innate immune responses (Gene ratio: 11.1%, adjusted $p = 2.84 \times 10^{-11}$; *MMP12, IL1A, LGALS9, LAG3, TICAM2*), and defense against viruses, for instance *OAS1A, EIF2AK2, OAS1A, MX1, CXCL10, DHX58*, and *IRF7* (Gene ratio: 13.9%, adjusted $p = 8.64 \times 10^{-14}$), whereas downregulated genes were over-presented by proteoglycan biosynthesis process (adjusted $p < 0.05$; *NDST3, NDST4*; Supplementary Fig. 2b). Kyoto Encyclopedia of Genes and Genome (KEGG) pathway analysis further corroborated these findings, highlighting the enrichment of innate immune response pathways (e.g. Toll-like receptor and NOD-like receptor pathways) and responses against viruses infections (e.g. COVID-19, Influenza A, Epstein-Barr virus) in upregulated genes (adjusted $p < 0.0001$), and lipid synthesis within the downregulated genes (adjusted $p < 0.05$) (Supplementary Fig. 2c). Amongst the significantly affected genes (FDR < 0.05), G86R mice displayed enhanced expression in inflammatory cytokines (Log$_2$FC ≥1; *IL12, IL6, TNF*) and chemokines (Log$_2$FC ≥ 1; *CXCL10, CCL5*). Furthermore, mirroring the G93A model at P84, G86R mice displayed robust enhanced expression of IFN-I and IFN-II (*IFNB1, IFNG*) and ISGs (*MX1 OASL1, IFI44, IRF7, ISG15*) at the P95 onset stage as well (Supplementary Fig. 2d). This inflammatory response was accompanied by activation of both astrocytes and microglia, as evidenced by increased expression of characteristic markers. Microglia displayed upregulation of *FCRLS, CD68, CD14, CD80, CX3CR1, P2RY12*, and *TMEM119*, while astrocytes exhibited increased expression of *GFAP, SOX9*, and *AQP4* (Supplementary Fig. 2d). INTERFEROME analysis confirmed the presence of ISGs, while only 2 out of 10 downregulated genes were IFN-I-induced

ISGs, a substantial portion (58%) of upregulated genes (175 out of 302, $P_{Fisher} = 9.39 \times 10^{-36}$) were classified as ISGs. Among these, 31 were specifically regulated by IFN-I, and 144 by both IFN-I and IFN-II. No IFN-III-induced genes were identified (Supplementary Fig. 2e). These findings demonstrate a consistent, mutation-independent upregulation of IFN-associated genes at the onset stage in SOD1-linked ALS models.

ATF3, CCL9, CCN1, SPRR1A, and TIMP1 serving as the biomarker for SOD1-ALS

To identify potential contributors to disease onset in the G93A model, we analyzed shared gene expression changes across asymptomatic (P28, P56) and onset stages (P84). While no differentially upregulated genes overlapped between P28 and P56, 14 of the 93 significantly upregulated genes at P56 (15%, FDR < 0.05) showed sustained overexpression at P84 (Fisher's exact test $P = 5.6 \times 10^{-52}$) (Fig. 2g, *upper*). Among these, the IFN-induced ISG *IFI44* displayed the most substantial increase, rising approximately 4.3-fold from P56 (mean FC = 6.23, FDR < 0.05) to P84 (mean FC = 27.1, FDR < 0.05). This was followed by tissue inhibitors of metallopeptidase inhibitor 1 (*TIMP1*), with a 2.5-fold increase from P56 (mean FC = 5.73) to P84 (mean FC = 14.22) (Fig. 2g). Matrix metalloproteinases (MMPs) degrade extracellular matrix components and contribute to demyelinating diseases by disrupting the blood-brain barrier, facilitating inflammatory cell migration, cytokine release, and myelin sheath breakdown[34]. Their activity is regulated by tissue inhibitors of MMPs (TIMPs), and an imbalanced MMPx:TIMP1 ratio is associated with various neurological disorders, including multiple sclerosis, showing a strong correlation with clinical score and demyelination[35–38]. Although not significantly altered at P28 and P56, both *MMP12* and *MMP19* displayed significantly increased expression at P84 in G93A model (mean FC = 14.72, FDR < 0.05 for *MMP12*; mean FC = 3.3, FDR < 0.05 for *MMP19*). Therefore, the upregulation of *TIMP1* at P56, followed by a significantly increased MMP12/19:TIMP1 ratio at P84 may suggest a progressive immune cell infiltration and potential myelin loss in the G93A model. In addition, *ATF3, SPRR1A, FMOD, RBP1*, and another ISG, *IFIT3*, were modestly upregulated (≈ 2-fold) at P84 relative to P56. While other genes (*ADA, NRROS, SH3BP2, CCL9, CCN1, ZFP36, SRGN*) showed significant increases at their respective time points, their P84/P56 ratios remained unaffected (Fig. 2g, *upper*). In contrast, only amine oxidase, copper containing 3 (*AOC3*) showed sustained downregulation from P28 (mean FC = −37.27, FDR < 0.05) to P56 (mean FC = −203.66, FDR < 0.05), with a robust 5.5-fold decrease. Notably, this decrease was not sustained at P84 (Fig. 2g, *lower*), suggesting a potential restoration towards WT levels as the disease progresses. Furthermore, no downregulated genes overlapped between P56 and P84 (Fig. 2g, *lower*), implying that downregulation is stage-specific and transient, with distinct genes affected at different time points during the early to onset stages in the G93A model.

To identify shared transcriptional patterns between the G93A and G86R models, we compared gene expression changes in their respective stages (G93A: P28-P56, G86R: P95). Of the 96 upregulated genes in the asymptomatic G93A model, 10 (10.4%) were also significantly upregulated in the G86R model at P95. These genes include those involved in cellular communication network (*CCN1, CCN5*), inflammation (*TIMP1, CCL9, ATF3*), structural roles (*SPRR1A, NES, TAGLN*), and the IFN response (*IFIT3, IFI44*) (Supplementary Fig. 2f, *upper*). Notably, six of these genes (*TIMP1, ATF3, IFIT3, IFI44, CCN1, SPRR1A*) remained persistently upregulated through the P84 onset stage in the G93A model (Supplementary Fig. 2g). Conversely, only one gene, N-Deacetylase and N-Sulfotransferase (*NDST4*, involved in hydrolase and deacetylase activity), overlapped between the downregulated clusters of the asymptomatic G93A stage (P28-P56) and the P95 stage in the G86R model (Supplementary Fig. 2f, *lower*).

To further substantiate the presence of IFN and ISG signatures in ALS SOD1 models, we re-analyzed another publicly available RNA-seq dataset of lumbar spinal cord tissue derived from G93A mice at disease onset (P90)[39] (Supplementary Fig. 3a). Using a significance threshold of |Log$_2$-FC| ≥ 1.0 (FDR < 0.05), we identified 124 DEGs, with 113 upregulated and 11 downregulated in G93A mice compared to WT controls. Among the top

significant hits, the volcano plot consistently highlighted previously confirmed genes associated with SOD1 pathology, including *CLEC7A* (FDR = 1.06 × 10^{-7}; $p = 3.65 \times 10^{-7}$), *TREML2* (FDR = 0.00344; $p = 1.13 \times 10^{-4}$), *TYROBP* (FDR = 1.29 × 10^{-7}; $p = 2.13 \times 10^{-5}$), and *CH25H* (FDR = 0.00344; $p = 6.8 \times 10^{-5}$) (Supplementary Fig. 3b, *left*). Unbiased functional enrichment analysis for biological processes revealed that upregulated genes were most significantly associated with immune cell regulation and cytokine activation (adjusted $p < 0.001$). KEGG pathway analysis further implicated pathways involved in cytokine receptors interactions, responses to viral components, and bacterial infection (adjusted $p < 0.05$, Supplementary Fig. 3b). This aligns with our previous observations and reinforces the role of dysregulated innate immune responses in SOD1 transgenic mice pathology. Given these findings, we then investigated the relationship between the DEGs and IFN pathways. Of the 113 differentially upregulated genes, 56 (49.6%, $P_{Fisher} = 3.91 \times 10^{-41}$) genes are classified as ISGs (e.g. *CH25H, IFI204, IFI207*), representing a significant portion of the analyzed gene pool. Specifically, 21 genes were regulated by IFN-I, and 35 genes by both IFN-I and IFN-II. None were regulated specifically by IFN-II or -III (Supplementary Fig. 3c). Furthermore, this G93A dataset consistently recapitulated enhanced expression of several chemokines (e.g. *CCL3, CCL4, CCL6, CCL9, CXCL16*), microglia activation markers (e.g. *FCRLS, CD68, ITGAX/CD11C*), and an increased in MMP12:TIMP1 (mean FC = 151.9:7.2) ratio.

We further investigated transcriptome alterations across different stages to identify potential contributors specifically associated with disease onset. By comparing data across time-points ranging from P28 to P90 in the G93A model, we obtained a more comprehensive landscape of gene expression changes at the onset stages. Remarkably, five genes (*CCN1, SPRR1A, CCL9, TIMP1*, and *ATF3*) showed significant upregulation starting from the asymptomatic stage (P56) and maintained high expression levels at P84 and P90. In contrast, of the 302 genes upregulated at P84, only 66 remained elevated at P90 (Supplementary Fig. 3d). The consistent upregulation of the aforementioned five genes in the G86R model at P95 suggests a potential common disease-related molecular signature associated with ALS onset in SOD1 models. Further characterization using INTERFEROME database revealed that 59% (42 out of 71, $P_{Fisher} = 1.10 \times 10^{-35}$) of these shared genes were ISGs, with ~66.7% co-regulated by both IFN-I and -II, and 33.3% specifically regulated by IFN-I. No genes were exclusively regulated by IFN-II or IFN-III (Supplementary Fig. 3d, *right*). Interestingly, *CCN5*, a connective tissue growth factor involved in WNT-signaling, exhibited an oscillatory expression pattern in G93A mice, closely mirroring the dynamic fluctuations observed in Cluster 3 genes. Its expression increased at the asymptomatic stage (P56), declined at onset (P84), and re-emerged at P90, following the same transient rise-and-fall pattern characteristic of Cluster 3. Unbiased GO analysis identified Cluster 3 enriched for genes involved in sprouting angiogenesis (Fig. 1d), a process in which CCN5 plays a known role. This alignment suggests its involvement in angiogenic remodeling during disease progression. Notably, no genes showed consistent downregulation across all time-points (P28-P90) in G93A (Supplementary Fig. 3d, left). Collectively, these findings suggest that the enhanced expression of IFN-I and -II ISGs during SOD1-linked ALS (both G93A and G86R) onset represents a consistent physiological response rather than a spontaneous event.

Persistent activation of IFN-I and IFN-II responses at the SOD1-ALS symptomatic stage

IFNs are pivotal in antiviral defense, yet their dysregulated activity contributes to autoimmune diseases by fostering a pro-inflammatory milieu through the induction of inflammatory mediators and the activation of immune effector cells[40]. Our data indicate their involvement in early ALS disease progression. To gain a more comprehensive understanding of their role in ALS pathogenesis, we performed RT-qPCR on brain and spinal cord tissues from WT and G93A mice at 10 (asymptomatic) and 20 (symptomatic) weeks of age. We observed a significant upregulation of several ISGs, including *ISG15, MX1*, and *IFIT1*, and chemokines, including *CXCL10, CCL2*, and *CCL5*, in both tissues of G93A mice compared to WT controls

(Supplementary Fig. 4a, b). This upregulation was more pronounced at 20 weeks of age, indicating a progressive increase in IFN signaling during disease progression. Furthermore, we observed increased expression of *IFNG* and *IFNB1* in the spinal cord and brain of G93A mice (Supplementary Fig. 4c). ELISA analysis confirmed elevated serum IFN-γ levels in G93A mice at both 10 and 20 weeks of age (Supplementary Fig. 4d). These results validate our initial RNA-seq analysis and demonstrate clear activation of both IFN-I and IFN-II signaling pathways in the G93A mouse model of ALS.

However, a comprehensive understanding of their role necessitates longitudinal studies encompassing both early and late symptomatic phases. To this end, we examined differential gene responses from symptomatic to terminal stages (P119-P150) in the G93A model. Our analysis revealed dysregulation of 783 genes at P119 and 1,382 genes at P150 (Fig. 3a, b). Notably, upregulation was predominant, increasing from 750 genes at P119 to 1220 genes at P150. Meanwhile, downregulation also increased with disease progression, from 16 genes at P84 to 33 at P119, and 162 at P150 (Fig. 3a, b). Most upregulated genes at these stages implicate pathways associated with immune activation in response to infections. This includes NF-kB signaling, cytokine-receptor interactions, and infections by pathogens such as Epstein-Barr virus, *Mycobacterium tuberculosis*, *Bordetella pertussis*, and *Trypanosoma cruzi* (the causative agent of Chagas disease). Autoimmune condition such as rheumatoid arthritis was also noted (Fig. 3c). It is important to note that IFN-II signaling and IFN-γ production are linked to infections like Chagas, tuberculosis and pertussis, whereas IFN-I is primarily associated with viral infections and the pathogenesis of rheumatoid arthritis[41]. Using GO analysis, we continued to observe a predicted activation of inflammatory and antiviral signaling pathways in both groups. This includes NF-kB signaling for TNF superfamily cytokine production (*CLEC7A, TREM2, TNFRSF1A, TYROBP*, adjusted $p = 2.45 \times 10^{-18}$) and the induction of IFNs and ISGs in response to viruses (*APOBEC1, IFI30, IFI207, MX1, CH25H, EIF2AK2, IFIH1, IFITM1*; adjusted $p = 5.6 \times 10^{-15}$) (Fig. 3d). Furthermore, we also observed the activation of brain-resident immune cells, including myeloid and leukocyte populations (*AIF1, CST7, C1QA, ITGB2, CD84, CX3CR1*; adjusted $p = 2.17 \times 10^{-21}$). These were evidenced by marked increases in the expression of relevant markers, starting at P84 and peaking at P119 and P150 (Fig. 3d, Supplementary Fig. 1c). In line with previous studies, several well-known ALS genes were successfully recapitulated (e.g. *TREM2, APOE, CX3CR1, KIF5A, CHODL*). Nevertheless, throughout these symptomatic stages, the G93A model demonstrated significant repression of genes associated with neuron synapses, skeletal and respiratory muscle development (Supplementary Fig. 1d). Examples include *SMYD1* (mean FC = −5.15, $p = 6.5 \times 10^{-5}$), *HEYL* (mean FC = −4.91, $p = 4.56 \times 10^{-8}$), *SIX4* (mean FC = −3.03, $p = 1.62 \times 10^{-5}$), *GLI1* (mean FC = −3.23, $p = 1.58 \times 10^{-6}$), *GNG8* (mean FC = −2.09, $p = 8.04 \times 10^{-5}$), and *RSPO2* (mean FC = −4.23, $p = 2.54 \times 10^{-9}$) (Supplementary Fig. 1d). This repression correlates strongly with the progression of severe limb paralysis observed in the animal model prior to its end stage at P150.

We then examined the temporal profiling across six time-points and observed that the majority of inflammatory response genes, chemokines, and ISGs began to show pronounced upregulation at the onset (P84) in the G93A, reaching a peak during the symptomatic stage (P119-P150). IFN-I (*IFNB1*) started to show modest upregulation as early as P56, gradually increasing at P84 and maintained an elevated level until P119, with a substantial surge observed at P150. In contrast, IFN-II signaling (*IFNG*) began modest upregulation at P56, peaked at P84, and sustaining until P119 before declining to WT levels at P150 (Fig. 3e, *middle*). It is important to note that ISGs induction requires the activation of secondary IFN-α/β/γ-receptor and JAK-STAT pathway, the temporal expression of ISG mRNA closely mirrored that of IFN-β and IFN-γ, with differential induction beginning modestly at P56, rising at P84, and maintained elevation until P150 (Fig. 3e, *right*). This pattern highlights that these genes are part of the group characterized by expression dynamics in Cluster 4. These ISGs constituted a significant proportion of the upregulated genes across symptomatic stages, accounting for 39.5% (296 out of 750, $P_{Fisher} = 1.58 \times 10^{-160}$) at P119, and 33.7% (411 out of 1,220,
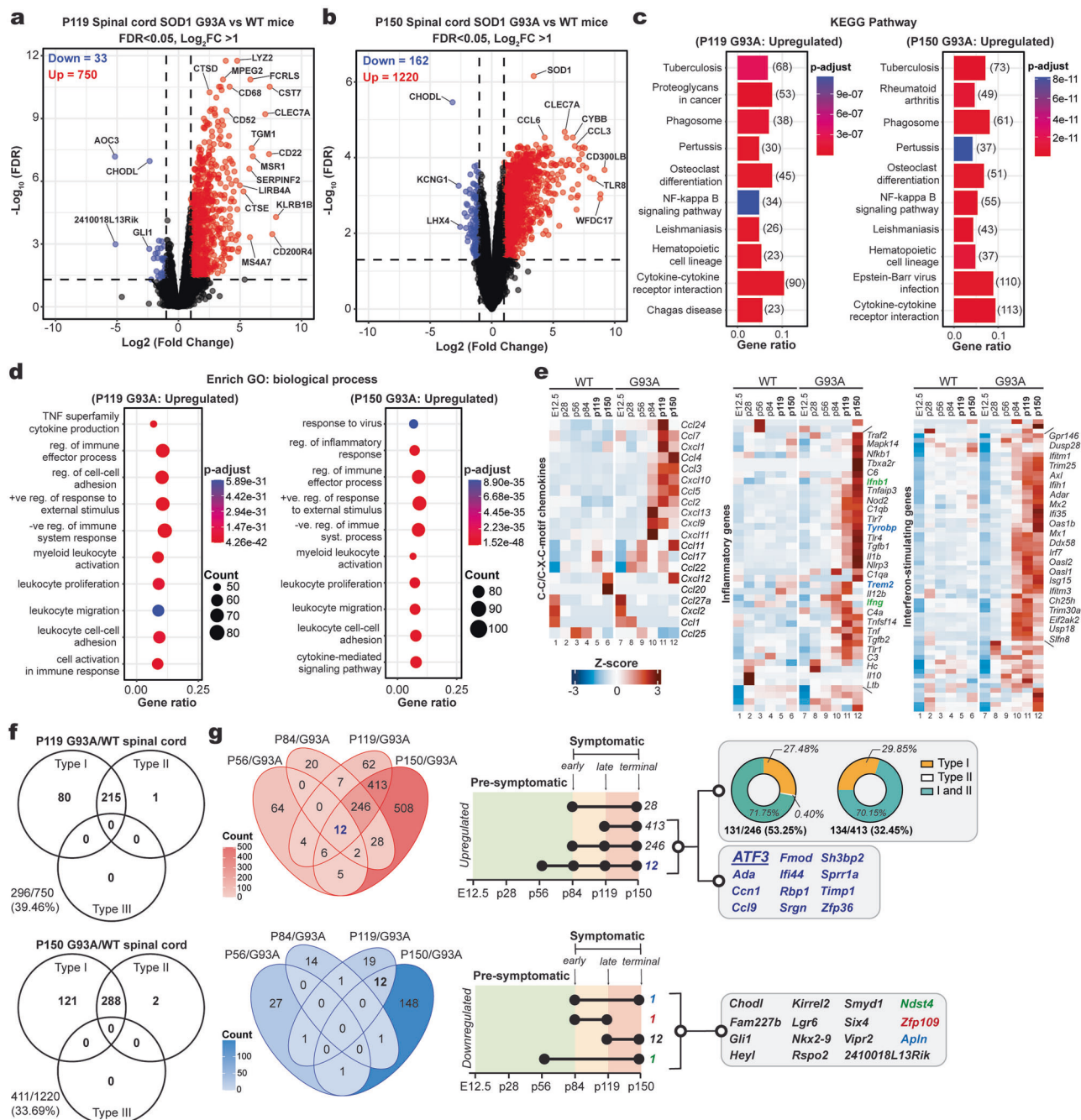
Fig. 3 | Enhanced expression of master transcriptional repressor ATF3 across ALS stages. Volcano plots of normalized differentially expressed genes from whole spinal cord of G93A over WT mice at postnatal day 119 (P119; n = 4 per group) (**a**), and day 150 (P150; n = 3 per group) (**b**). (*Dotted lines*: Log2 = 1/-1, 2-fold expression changes). **c** Top ten significant enriched KEGG pathways of the up-regulated DEGs from both P119 and P150 G93A/WT. The number of genes associated with each pathway is indicated beside the corresponding bar. **d** Enrichment pathway analysis of Biological Process (BP) GO terms of upregulated DEGs in both P119 and P150 G93A/WT mice. **e** Heatmap of selected chemokines, pro-inflammatory, and interferon-stimulating genes in G93A versus WT mice ranging from E12.5 to P150. (Blue: *TYROBP* and *TREM2* are positive control for upregulated genes in G93A model) (**f**) The Venn diagram illustrates the classification of up-regulated DEGs from G93A/WT at P119 and P150 mice into categories of Type I, II, and/or III ISGs. **g** (*left*) Venn diagram illustrates the genes that overlap across from P56 to P150 of G93A/WT mice; (*right*) the upset matrix plot displays the total number of DEGs identified in E12.5-P150 of G93A mice. The pie chart shows the percentage of DEGs from their respective temporal profiles that are categorized as Type I and/or II ISGs in the CNS. Examples of genes corresponding to specific time-points are color-coded accordingly.

$P_{Fisher} = 5.73 \times 10^{-185}$) at P150. The majority of these genes were co-regulated by both IFN-I and IFN-II [72.6% (215/296 genes) at P119, and 70.1% (288/411 genes) at P150]. A subset was specifically regulated by IFN-I [27% (80/296) at P119, 29.4% (121/411 at P150)], with a small fraction by IFN-II (1/296 at P119, and 2/411 at P150) (Fig. 3f). Despite previous research indicating that IFN-I and IFN-III induce a similar set of ISGs[42], we observed no dysregulation of IFN-III (IFN-λ) signaling in G93A compared to WT across all time-points.

This finding corroborates the absence of shared or IFN-III-specific ISGs in G93A across all time-points (Fig. 3e, f), suggesting that both IFN-β and IFN-γ, but not IFN-λ, are the primary drivers of ISGs induction in the SOD1 mutant model.

Continuous comparative analysis of gene expression profiles across disease stages has revealed a set of overlapping genes with distinct expression patterns potentially critical for disease onset and progression. In contrast to the

earlier downregulation observed from P28 to P84/P90, 12 genes associated with synapses and muscle development were downregulated from P119 and remained attenuated at P150 (Fig. 3g, *lower*). The upregulated gene cluster, on the other hand, exhibited two distinct phases of widespread gene expression changes. Specifically, 28 genes displayed an oscillatory expression pattern (Cluster 3), characterized by upregulation at P84, restoration to WT levels at P119, and subsequent upregulation again at P150. Another 413 genes showed enhanced expression from P119 to P150, while 246 genes were continuously upregulated from P84 to P150 (Fig. 3g, *upper*). Importantly, a significant portion of these upregulated genes across symptomatic stages were IFN-I, IFN-II, and their downstream ISGs. This included 53.25% (131 out of 246, $P_{\text{Fisher}} = 5.39 \times 10^{-97}$) of genes at P84-P150 and 32.45% (134 out of 413, $P_{\text{Fisher}} = 8.47 \times 10^{-66}$) at P119-P150. Moreover, 170 upregulated genes shared between P84-P150 in G93A were also upregulated in G86R model at P95. These shared genes were enriched in innate and adaptive immune pathways, particularly Toll-like receptor and IFN signaling (Supplementary Fig. 2g). Notably, 67% (114 out of 170, $P_{\text{Fisher}} = 2.41 \times 10^{-101}$) of these shared genes were ISGs, with 78.9% (90/114) co-regulated by IFN-I and II, and 21% (24/114) by IFN-I alone (Supplementary Fig. 2h). This emphasizes the prevalence of ISGs and other immune-related genes across different disease stages and SOD1 mutations. A core set of 12 genes (*ATF3, ADA, CCN1, CCL9, FMOD, IFI44, RBP1, SRGN, SH3BP2, SPRR1A, TIMP1, ZFP36*) displayed persistent upregulation in the G93A model, spanning from the pre-symptomatic stage (P56) through disease onset (P84) and into late symptomatic phases (P119, P150). Several of these genes are ISGs (*ATF3, CCL9, IFI44, TIMP1, ZFP36*). Importantly, five of these genes—*CCN1, SPRR1A, CCL9, TIMP1,* and *ATF3*—displayed the same persistent upregulation across disease stages in both G93A and G86R models (Fig. 2). Their sustained elevation in G93A model through P119 and P150 (Fig. 3g, *upper*) highlights their potential as markers of both disease onset and progression. We propose the term "*SOD1-ALS Associated Signature*" (SAAS) to describe this marker set, as their appear to represent a consistent signature of disease across SOD1-linked ALS.

The examination of transcription factor activity changes across SOD1 mutant genetic backgrounds using the TF2DNA database[43] ($p < 0.0001$) revealed significant alterations in 17 transcription factors in both G86R and G93A mice. These included changes in *NFIL3, JUN, HEY2, OLIG3, DBP, SP110*, members of the fos-like antigen family (*FOSL1, FOSL2*), members of the IRFs family (*IRF1, IRF5, IRF7, IRF8, IRF9*), and members of the CCAAT/enhancer-binding protein (C/EBP) family (*CEBPA, CEBPB, CEBPD*). Several IRF members are ISGs regulated by a positive feedback loop involving IRF3 and IFN-α/β/γ-receptor signaling. Among these, *IRF8* displayed the most significant upregulation (mean FC = 11.55, $p = 1.06 \times 10^{-8}$) as the disease progressed (Supplementary Fig. 5). Of particularly interest, the transcription factor ATF3 (a SAAS member) displayed consistently enhanced expression in both G93A and G86R models. This upregulation began as early as P56 and persisted throughout disease progression, reaching a mean FC of ~5.3 at onset (P84), ~11.7 in the symptomatic stage (P119), and remained highly elevated at P150 (~40.4) (Fig. 3g, Supplementary Fig. 3d and 5). ATF3, a member of the ATF/cAMP response element-binding (CREB) family, functions as both an activator and repressor of cellular homeostasis and immune responses. It forms homo/heterodimers with bZIP-domain containing proteins, including activating protein 1 (AP-1), and C/EBP family members[44]. Importantly, C/EBPδ (encoded by *CEBPD*) promotes inflammatory signaling, whereas CEBPα (encoded by *CEBPA*) exhibits anti-inflammatory properties. C/EBPδ expression is typically transient and is downregulated by ATF3 in a negative feedback loop to mitigate inflammation[45,46]. Our analysis revealed pronounced and sustained *CEBPD* upregulation in SOD1-ALS model (mean FC = 10, FDR < 0.05) from onset stage (P84) to the terminal stage (P150) (Supplementary Fig. 5). While a similar *CEBPA* upregulation trend was observed at G93A time points, it was absent in G86R (P95) and an independent G93A dataset (P90) (Supplementary Fig. 5). The persistent enhancement of ATF3 and *CEBPD* suggests potential roles for ATF3 and ATF3-C/EBPδ, and possibly ATF3-AP-1/FOSL complexes, in disease progression. Our findings indicate that altered transcription factors activity may modulate the magnitude and duration of inflammatory signaling across

different phases through a network of mutual regulatory feedback loops in SOD1-ALS model.

Substantial decrease of neuron cells in the spinal cord of SOD1-ALS

While our bulk transcriptomic analyses of CNS tissues consistently revealed elevated expression of ISGs in ALS, this approach lacks the resolution to identify the specific cell types responsible for this ISG signature. To our knowledge, no prior studies have integrated single-nucleus transcriptomics in the meta-analysis of SOD1-linked ALS. Therefore, we analyzed G93A mice at disease onset (P90) using single-nuclues RNA-seq (snRNA-seq) to investigate the contributions of different cell subsets to the inflammatory microenvironment in SOD1-associated ALS. After integrating snRNA-seq data from the spinal cord tissue of WT and G93A mice[47], we filtered out low-quality cells and doublets (Supplementary Fig. 6), retaining 14,662 high-quality single cells that passed quality control. This allowed us to recover an average of 3000 genes per cell and a mean of 30,000 unique molecular identifiers (Supplementary Fig. 6a). We then annotated these cells using canonical lineage markers to discriminate subpopulations, with further confirmation using Azimuth[48]. Unsupervised clustering based on t-distribution stochastic neighbor embedding (t-SNE) after normalization and batch-effect correction resolved distinct major cell types, including astrocytes (*GFAP, SLC1A3, SCL4A4, FGFR3, ATP13A4*), neurons (*TSHZ2*), microglia (*CX3CR1*), pericytes (*ABCC9, VTN*), vascular cells (*FLT1, PECAM1, TEK, MYL9*), oligodendrocytes (*SOX10, PDGFRA, MOG*), and oligodendrocytes precursor cells (OPC; *NG2, PDGFRA*) (Fig. 4a, Supplementary Fig. 7). Among these, neurons and oligodendrocytes were the primary cell types identified, accounting for 65.64% and 18.76% of the total population, respectively. Astrocytes constituted 10.67%, vascular cells 3.34%, OPC 1.16%, pericytes 0.37%, and microglia 0.06% (Fig. 4b). Within the neuronal compartment, we identified canonical subpopulations of GABAergic neurons expressing vesicular inhibitory amino acid transporter (encoded by *SLC32A1*), and glutamatergic neuron cells expressing N-methyl-D-aspartate receptor (encoded by *GRIN1*). Both neuron types may also shared some expression markers such as synaptic vesicle glycoprotein 2c (*SV2C*). The vascular cell compartment primarily consisted of *LY6C1*-expressing endothelial cells (Fig. 4c, Supplementary Fig. 7). Housekeeping genes *GAPDH* and *ACTB* served as controls, showing consistent expression across all clusters (Supplementary Fig. 7b). All cell types were identified across three biological replicates.

Next, we assessed whether genotypes influence changes in the absolute abundance of each cell population at the onset stage. Compared to WT controls, G93A mutant exhibited an expanded proportion of microglia (+25%; $P\chi^2 < 0.0001$) and pericytes (+3.70%; $P\chi^2 < 0.0001$; Fig. 4d), supporting the notion that immune cells infiltration had begun at the onset stage. This aligns with the previously observed increased expression of ISGs, chemokines, and microglia activation markers seen in bulk analysis. In contrast, we recorded a substantial reduction in neurons (−25.5%; $P\chi^2 < 0.0001$), and astrocytes (−19.88%; $P\chi^2 < 0.0001$). Further analysis of neuronal subtypes revealed significant decreased in both GABAergic and glutamatergic neurons (-27.58% and −22.7%, respectively; $P_{\text{Fisher}} = 0.0143$; Fig. 4d). This disruption also extended to OPC (−22.36%; $P\chi^2 < 0.0001$), oligodendrocytes (−7.38%; $P\chi^2 < 0.0001$), and vascular cells (−3.68%; $P\chi^2 < 0.0001$) in G93A mice (Fig. 4d).

Pronounced ISGs upregulation in vascular endothelial cells

Further characterization of the transcriptional differences between G93A and WT controls across all seven cell types identified 337 DEGs in at least one cell type. Of these, 303 were upregulated and 34 were downregulated in the mutant [|Log2FC| > 0.5; $P_{\text{adjusted}} < 0.05$; Fig. 4e]. Validating our bulk RNA-seq findings, GO enrichment analysis revealed that the upregulated module were enriched for processes related to the innate immune system and signaling via the JAK-STAT pathway (Fig. 4f). Conversely, the downregulated module across all cell types was enriched for functions associated with calcium ion transport (e.g. *GRIN2A, TSPOAP1, TRPC6*), ATPase binding (e.g. *ZNHIT6,*
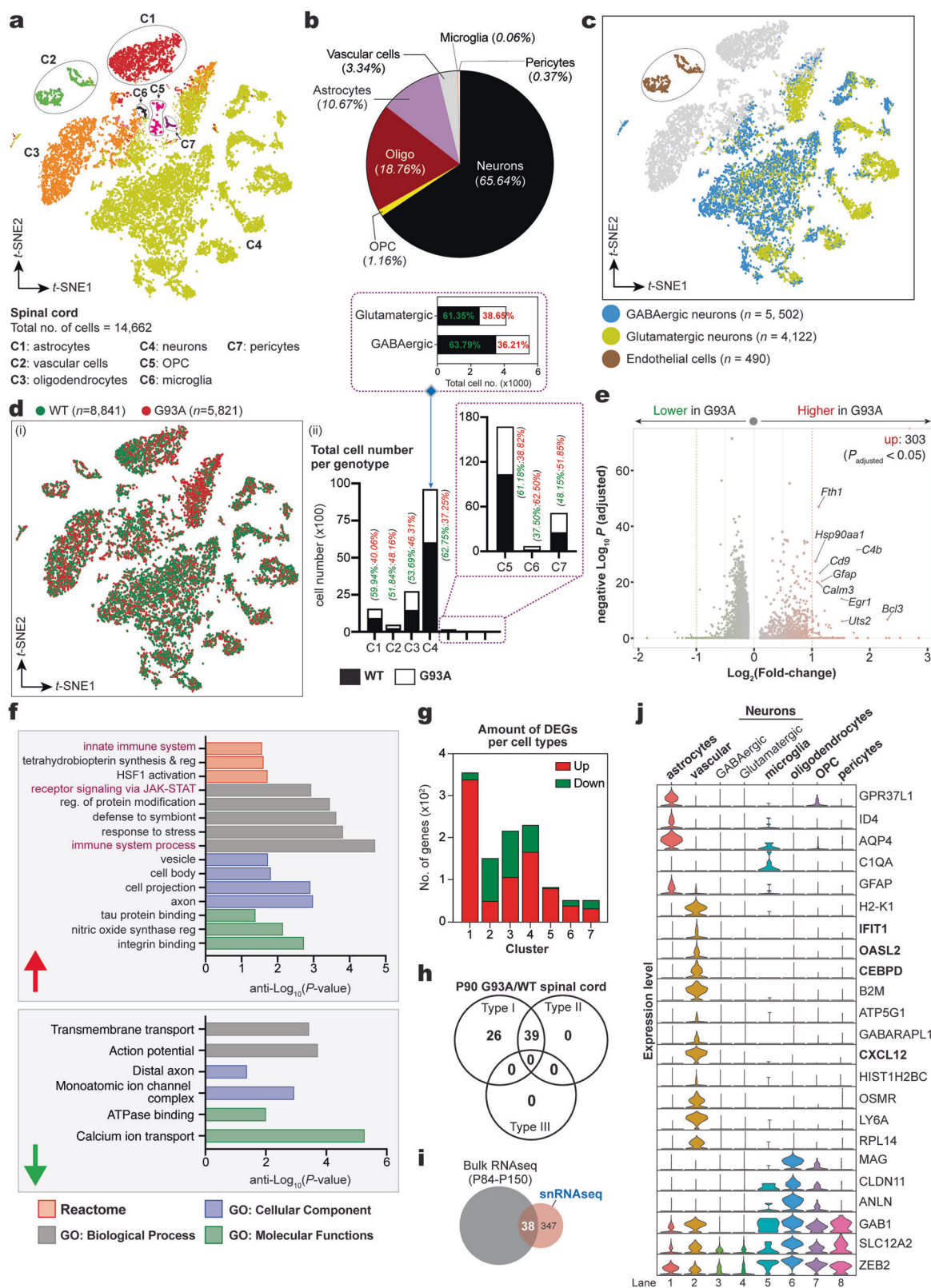
TRPC5, ESR1), and neuronal action potential (e.g. *TACR1, KCNH7, CHRNA7*) (Fig. 4f). Strikingly, although neurons being the most abundant of cell-types, astrocytes exhibited the highest number of DEGs between G93A and controls (31.25%), followed by neurons (20.25%) and oligodendrocytes (19%). Pericytes and microglia each contributed 4.5% of DEGs (Fig. 4g).

Motivated by the basal induction of ISGs observed in SOD1 mutants in our longitudinal bulk RNA-seq, we hypothesized this would also be evident at the single-nucleus level. Indeed, snRNA-seq analysis confirmed this, with 65 (16.88%, $P_{Fisher} = 3.66 \times 10^{-27}$) upregulated DEGs identified as ISGs. Of these, 39 were co-induced by IFN-I and IFN-II, while 26 genes were

Fig. 4 | Expression changes across seven cell types in SOD1-ALS. a t-SNE and assignment of 14,662 cells to 7 cell types: astrocytes (C1); vascular cells (C2); oligodendrocytes (C3); neurons (C4); OPC (C5); microglia (C6); and pericytes (C7). **b** Percentage for each cell type in G93A versus WT controls (*n* = 6 per group). **c** t-SNE of vascular and neurons populations reclustered into three subpopulations: endothelial; GABAergic neurons; and Glutamatergic neurons. Total number of cells for each subpopulation were indicated. **d** t-SNE projection (i) and percentage quantification (ii) of all seven major and subclustered cell types with genotyping data. **e** Volcano plot of differential gene expression [Log2(G93A/WT)] in G93A mutant vs WT control mice based on normalized gene expression values.

Significantly dysregulated genes [5% FDR (Benjamini-Hochberg-corrected *p*-value)] are indicated in red (upregulated; *red dotted line*: Log$_2$FC ≥ 1.0) and green (downregulated; *green dotted line*: Log$_2$FC ≤ -1.0). **f** Pathway analysis (GO) was performed using g:Profiler database (Reactome, Biological Process, Molecular Function, and Cellular Component). **g** The distribution of DEGs proportions across all cell clusters. Venn diagram illustrates the classification of ISGs upon analysis by INTERFEROME (**h**), and the shared DEGs between bulk and snRNA-seq (**i**). **j** Normalized expression values of indicated differentially expressed ISGs were plotted as violin plots with genes as rows and clusters as columns (*Lane 1-8*).

specifically induced by IFN-I. Mirroring our bulk analysis of murine datasets, no IFN-II and IFN-III specific ISGs were found (Fig. 4h). Furthermore, 38 (9.87%) DEGs from our time-course bulk analysis were also differentially expressed at the single-nucleus level (Fig. 4i), with 18 identified as ISGs. This suggests a similarity between the bulk tissue and single-nucleus data. Unexpectedly, despite astrocytes harboring the highest number of DEGs overall, vascular endothelial cells displayed the most robust upregulation of ISGs in terms of fold-change magnitude. Key antiviral ISGs—including *OASL2* (Log$_2$FC = 3.46, *p* = 8.21 × 10^{-7}), *IFIT1* (Log$_2$FC = 4.76, *p* = 1.05 × 10^{-5}) and *IFIT2* (Log$_2$FC = 1.21, *p* = 2.73 × 10^{-6})—were upregulated in endothelial cells at fold-changes exceeding those observed in other cell types. Vascular endothelial cells also showed prominent induction of *CXCL12* (Log$_2$FC = 1.87, *p* = 3.95 × 10^{-5}), a potent lymphocytes chemoattractant[49], and *CEBPD* (Log$_2$FC = 0.94, *p* = 9.23 × 10^{-5}), the transcription factor persistently elevated from disease onset to terminal stages in bulk datasets from both G93A and G86R models (Fig. 4j, *lane 2*). Microglia and astrocytes also differentially expressed some of these ISGs, albeit at lower fold-change magnitudes compared to vascular endothelial cells. In contrast, neurons showed minimal differential expression of ISGs in the G93A mutant (Fig. 4j, *lane 3 and 4*). This suggests that ISGs induction in these populations is either less pronounced or largely below the threshold of differential expression detection in this dataset. These distinct cell-type-specific expression patterns highlight the previously unappreciated and significant role of vascular endothelial cells in coordinating both IFN-I and -II responses in SOD1-associated ALS.

Post-mortem ALS tissue versus murine ALS model

To examine gene expression similarities and differences between mouse and human spinal cord regions, we conducted a comparative analysis using post-mortem spinal cord RNA-seq data from the NYGC ALS cohort. This dataset comprised samples from 421 ALS patients (223 cervical and 198 lumbar) and 105 controls (52 cervical and 53 lumbar regions) (Fig. 5a). For this purpose, our analysis focused on homologous genes shared between mice and human, identified through orthologous information from the NCBI HomoloGene system[50]. Following standard preprocessing and normalization procedures, differential expression analysis was performed by comparing the RNA-seq signals between ALS and control samples to identify aberrant gene expression in ALS. In the cervical region, 351 genes showed significant differential expression between post-mortem ALS and control spinal cord samples (FDR ≤ 0.05, |Log$_2$-FC| ≥ 1), with 205 upregulated and 146 downregulated (Fold ≥ 2; FDR < 0.05; Fig. 5b, *left*). Among the most highly upregulated genes were *CCL18* (mean FC = 25.46), *CHIT1* (mean FC = 19.84), LINC01857 (mean FC = 10.41), and *CHRNA1* (mean FC = 7.62). Conversely, *CXCL11* (mean FC = −11.24), *CSF3* (mean FC = −3.94), *VWA5B2* (mean FC = −3.01), *SLC1A7* (mean FC = −2.89), and microRNA 4534 (MIR4534, mean FC = −2.68) were among the most markedly repressed genes in ALS subjects. The lumbar region showed 438 DEGs, with 277 upregulated and 161 downregulated (Fold ≥ 2; FDR < 0.05; Fig. 5b, *right*). Here, highly upregulated genes included *XIRP2* (mean FC = 26.54), *CHIT1* (mean FC = 11.47), *CHRNA1* (mean FC = 9.0), and *DNAJC5B* (mean FC = 6.87). Notably, *CHIT1* and *CHRNA1* were consistently upregulated across both spinal cord regions. *CXCL11* (mean FC = −10.48) and *CSF3* (mean FC = −2.89) were again among the most downregulated genes

in the lumbar region. To understand the biological implications of these DEGs, we performed GO term enrichment analysis. In the cervical region, upregulated genes were primarily associated with immune-related pathways, including heightened activation of adaptive immune response. This included the regulation of immune effector process (*MR1, LGALS3, ACP5, SLAMF8*), T-cell activation (*TYROBP, CD84, IL18, FCER1G*; enrichment *p* = 2.2 × 10^{-7}); MHC Class II protein assembly (*HLA-DQA1, HLA-DRA, HLA-DRB5, HLA-DMB*; enrichment *p* = 6.3 × 10^{-7}), and antigen processing and peptide presentation (*CTSS, FCGR2B, HLA-DOA, HLA-DPB1*; enrichment *p* = 2.3 × 10^{-7}), indicating an enhanced antigenic presentation capacity (Fig. 5c). Notably, there was a strong enrichment in genes related to leukocyte chemotaxis (*CCL18, CCR7, CCL2, CCL20, CXCR4*; enrichment *p* = 2.3 × 10^{-7}), and mononuclear cell migration (*ANO6, PLA2G7, ANXA1, SERPINE1*; enrichment *p* = 2.0 × 10^{-7}; Fig. 5c, *left*) was also observed, suggesting active immune cell recruitment to the CNS. However, in autoimmune conditions, such infiltration could be detrimental, causing neuronal damage. Additionally, an increased expression of genes positively regulating cytokine production (*GPNMB, PTPN22, CR1, IL2RA, CD44*; enrichment *p* = 2.1 × 10^{-7}; Fig. 5c, *left*), indicating a pro-inflammatory environment in post-mortem ALS tissue.

Consistent with the cervical region, analysis of upregulated genes in the lumbar region revealed a strong association with immune-related pathways. This included leukocyte-mediated immunity (*IL18, CTSC, CD84, FCGR1A*; enrichment *p* = 3.9 × 10^{-5}), regulation of leukocyte differentiation (*FGL2, EVI2B, CD86, CCR1*; enrichment *p* = 4.3 × 10^{-5}), and positive regulation of T-cell activation (*VNN1, IGF1, HLA-DMA, HLA-DQA1*; enrichment *p* = 4.3 × 10^{-5}; Fig. 5c, *right*). Enhanced expression of *TYROBP, IL17B, LAPTM5* and *CYBB* within the cytokine production pathway (enrichment *p* = 2.7 × 10^{-5}, Fig. 5c, *right*) further supports a pro-inflammatory environment. Moreover, significant enrichment of genes linked to bacterial responses (*LY96, LY86, SCIMP, TLR5, TLR8*; enrichment *p* = 1.7 × 10^{-5}; Fig. 5c, *right*) suggests an active role for innate immune sensing pathways, such as those involving Toll-like receptors in promoting inflammation driven by cytokines, including IFNs, chemokines, interleukins and TNF family members. In contrast, downregulated genes in the lumbar region were enriched for functions related to cell locomotion, motility, migration, microtubule organization, and dynein assembly (enrichment *p* < 0.05; Fig. 5d; *right*). These processes are crucial for neuronal function, and their downregulation implies functional deficits contributing to neuronal dysfunction and death. The observed decrease in dynein expression is particularly notable, as dynein plays vital roles in mitochondrial movement[51], trafficking of vesicles and misfolded proteins[52], nuclear positioning[53], and mitosis[54]. Our findings align with existing literature that implicates dynein and microtubule dysfunction in ALS and other neurodegenerative diseases.

Shifting to the cervical region, we observed a preferential downregulation of transcripts involved in Ca^{2+} ions-mediated signaling (*CACNA1B, TRPV6, NTSR, GRIN1*), dendrites morphogenesis (*SRCIN1, SHANK1, SHANK3, CUX2*), and membrane depolarization (*CNGB1, HCN4*) (enrichment *p* < 0.02; Fig. 5d; *left*). These processes are crucial for efficient neurotransmission, and their downregulation suggests ALS-associated synaptic dysfunction and may contribute to neuronal hypoexcitability in motor neurons innervating muscle fibers.
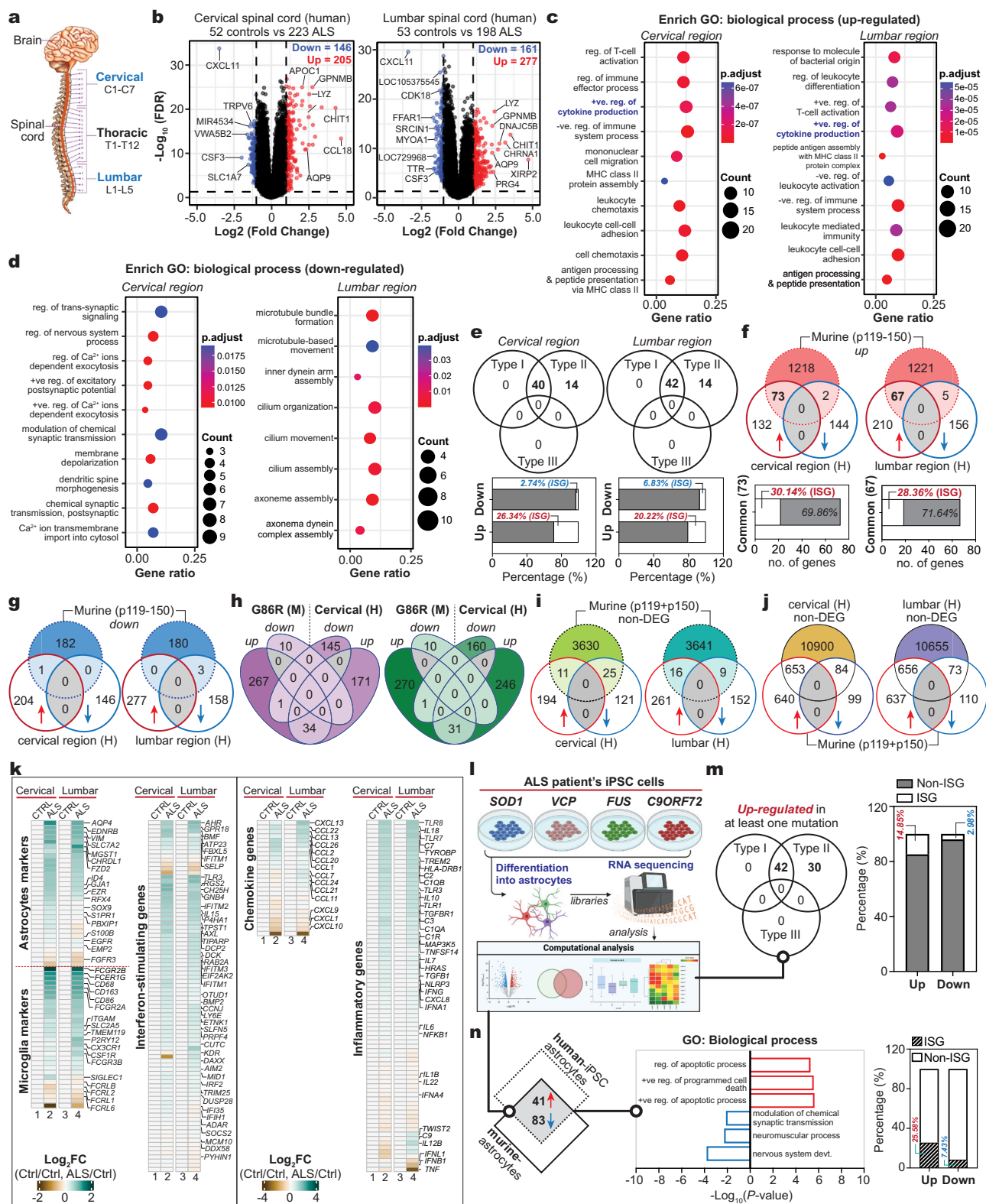
Fig. 5 | Enrichment of interferon-associated immune signatures in ALS hiPSCs and post-mortem spinal cord tissues. a Schematic representation of the human CNS illustrating the anatomical regions of the spinal cord, including the cervical, thoracic and lumbar regions. **b** Volcano plots of normalized differentially expressed genes ($|Log_2FC| \geq 1$, FDR < 0.05) in post-mortem ALS patient tissue obtained from cervical ($n = 223$ samples), and lumbar ($n = 198$ samples) spinal cord regions. **c, d** Enrichment pathway analysis of Biological Process (BP) GO terms of up- and down-regulated DEGs of the same tissues. **e, f** Analysis of significantly DEGs ($|Log_2FC| \geq 1$, FDR < 0.05) present in post-mortem ALS spinal cord relative to healthy controls via Interferome.org. **g–j** Comparison of either significantly or non-significantly altered genes ($|Log_2FC| \geq 1$, FDR < 0.05) of SOD1^{Mut} mice at terminal stage with post-mortem ALS samples relative to WT mice/healthy controls. **k** Heatmap of indicated genes in post-mortem ALS tissue compared to control samples. **l** Schematic depicting experimental workflow for transcriptomic datasets from ALS mutant hiPSC-astrocytes. **m, n** Comparison analysis of significantly altered genes across different ALS mutants of hiPSCs-astrocytes, as well as with murine species.

IFN-I and IFN-II ISGs expression in terminal stage of sporadic ALS patients

The IFN response, recently identified as a key driver of inflammation in ALS[14–16], has been extensively studied in mouse models. However, its relevance to human ALS, including sporadic cases, remains scarce. To address this knowledge gap, we sought to determine whether the upregulation of IFN-I and IFN-II-associated ISGs observed in SOD1 mutant mice also extends to human ALS. Beginning with sALS, we analyzed significantly upregulated genes from both cervical and lumbar region using the INTERFEROME database. Our analysis revealed that a significant portion of 26% (54 out of 205 genes, $P_{Fisher} = 1.57 \times 10^{-23}$) among the upregulated genes in the cervical region are ISGs. Similarly, approximately 20.2% (56 out of 277, $P_{Fisher} = 1.66 \times 10^{-18}$) of the upregulated genes in the lumbar region were identified as ISGs (Fig. 5e). As expected, the proportion of ISGs among downregulated genes was low (<10%), with just approximately 3% and 7% in the cervical and lumbar regions, respectively (Fig. 5e). To our surprise, a significant portion of ISGs showed exclusive dependence on IFN-II (IFN-γ) rather than IFN-I (IFN-α/β). Approximately 26% (14 out of 54) of upregulated ISGs in the cervical region and 25% (14/56) in the lumbar region were specifically regulated by IFN-II, with the rest co-regulated by IFN-I and IFN-II. Consistent with mouse models, IFN-III (IFN-λ) was not involved (Fig. 5e). This finding contrasts with murine ALS models, where a significant portion of ISGs are IFN-I dependent, suggesting that in terminal-stage sporadic ALS patients, IFN-II is the primary driver of ISGs expression.

We therefore initiated a comparative analysis of gene content between murine and human sporadic ALS transcriptomes to address the observed discrepancies. As the human dataset originated from terminal post-mortem spinal cord tissue, we selected P119-P150 terminal stage of the murine model for comparison. We first collated all upregulated genes (mean FC ≥ 2.0, FDR < 0.05) in the G93A model from P119 to P150, identifying 1293 significantly upregulated genes during the late stages. Comparing these genes to those upregulated genes in the human cervical and lumbar region revealed a modest overlap: only 73 genes (∽5.6%) in the mouse model were also upregulated in the human cervical region, and 67 genes (∽5.2%) in the human lumbar region (Fig. 5f, *upper*). In contrast, several genes displayed opposing expression patterns between two species. For examples, *CXCL10* and *NOTCH4* were upregulated in G93A model but downregulated in the human cervical spinal cord, and five upregulated murine genes were shared with the downregulated cluster in the human lumbar region (Fig. 5f, *upper*). Notably, a significant portion of these shared genes are ISGs, comprising approximately 30.14% (22/73, $P_{Fisher} = 6.61 \times 10^{-12}$) in the cervical region and 28.36% (19/67, $P_{Fisher} = 5.48 \times 10^{-10}$) in the lumbar region (Fig. 5f, *lower*). The relatively low percentage of shared upregulated genes prompted us to consider the possibility that the non-overlapping genes found in humans might be downregulated in the murine model.

However, comparing the significantly downregulated genes in G93A murine model against the human transcriptome revealed no significant shared genes with the upregulated gene clusters in either the cervical or lumbar regions (Fig. 5g). This suggests that opposing gene regulation in the mouse does not account for the limited overlap. The downregulated gene cluster in the late-terminal G93A model also showed minimal similarity to the human downregulated profile, with only three genes (*RGS11, GRID2IP, CFAP46*) shared between the G93A model and the human lumbar spinal cord (Fig. 5g). We also compared the G86R murine model at P95 to human ALS. Despite disease stage differences, we consistently observed shared upregulated genes with both the cervical (∽11.3%, 34 genes) and lumbar (∽10.3%, 31 genes) regions (Fig. 5h). This group includes a substantial number of ISGs, such as *SLAMF8, ADORA3, CD84, CD86,* and *RNASE4*. Similar to the G93A comparison, no shared downregulated genes were found (Fig. 5h). Collectively, our findings suggest that mice and human ALS models consistently share a small subset of upregulated genes, many of which are ISGs. However, both species clearly exhibit distinct dysregulated expression profiles within both up- and downregulated clusters, irrespective of disease stage or mutation type.

We hypothesized that genes significantly differentially expressed in human ALS might not show differential expression in mice during the late terminal stage. To test this, we compared human DEGs with genes in mice identified as statistically significant but not differentially expressed (FDR < 0.05, mean FC ≤ 2.0). We found a minor overlapped between these mouse genes and upregulated genes in human: 5.4% (11 out of 205 genes) in the cervical region and 5.8% (16 out of 277 genes) in the lumbar region (Fig. 5i). On the contrary, although the percentage remained small, we observed a slightly higher number of genes within the non-DEGs cluster in mice corresponding with the downregulated cluster in humans, accounting for 17.1% (25 out of 146 genes) in the cervical region, and 5.6% (9 out of 161 genes) in the lumbar region (Fig. 5i). This limited overlap suggests that non-differential expression in mice does not fully explain the differences between human and mouse ALS gene expression profiles. Therefore, we investigated whether DEGs from the late terminal stage of murine G93A model were non-differentially expressed in human ALS samples. Of the 11,637 genes classified as significant but not differentially express in human cervical spinal cord, 653 genes shared with the upregulated gene cluster in the P119-P150 stage of the G93A model. This represents 50.5% (653 out of 1293 genes) of the upregulated cluster in the G93A model, a substantial increase compared to only 5.6% (73 out of 1293 genes) shared with the upregulated cluster of the cervical spinal cord region (Fig. 5j, *left*). Similarly, 50.7% (656 out of 1293 genes) of the upregulated cluster in G93A model overlapped with the non-DEG in human lumbar region, a drastic increase of 26.5% (589 genes) compared to only 5.2% (67 out of 1293 genes) shared with the upregulated cluster in lumbar region (Fig. 5j, *right*). A similar trend emerged in the analysis of downregulated cluster. Approximately 45.9% (84 out of 183 genes) of downregulated G93A genes overlapped with non-DEG in the human cervical region (Fig. 5j, *left*). This represents a drastic increase compared to the absence of overlap with downregulated cervical cluster. In contrast, a smaller yet substantial 39.8% (73 out of 183 genes) of downregulated G93A genes overlapped with non-DEGs in lumbar region. This highlights a pronounced 38.2% (70 genes) difference relative to the minimal 1.6% (3 out of 183 genes) shared with the downregulated lumbar cluster (Fig. 5j, *right*). These results suggest that the limited shared DEGs between human sporadic ALS and the G93A model primarily stem from the human orthologs of murine DEGs showing no significant change in expression between human ALS cases and healthy controls, despite the shared disease phenotype. This highlights distinct species-specific gene expression profiles, even at comparable disease stages. Therefore, translating findings from mouse models to human ALS requires careful interpretation and consideration.

Nevertheless, broad characterization of transcriptomic effects reveals close resemblance between human post-mortem ALS spinal cord cohort and the murine model across disease progression (P84-P150). This similarity is particularly evident when examining upregulated biological processes identified through GO analysis. Genes and pathways consistently upregulated throughout this disease continuum are predominantly associated with immune response, including immune cell activation, IFN-I (*IFNA1*, *IFNA4*, *IFNB1*) and IFN-II (*IFNG*) signaling, and chemokine production (Fig. 5k). These findings suggest widespread immune hyperactivation within the ALS spinal cord region, further corroborating the presence of a highly inflammatory systemic immune signature in both human and mouse ALS models.

iPSC-derived astrocytes resources

The limited availability of relevant human tissue samples remains a major challenge in ALS research. While post-mortem spinal cord tissues provide valuable insights, they represent end-stage disease with significant cell loss. To overcome this limitation and study the disease processes in a more controlled setting, we utilized hiPSCs. These versatile cells can be differentiated into various disease-relevant cell types, allowing us to model the complex etiology of ALS in vitro. Furthermore, using hiPSCs derived from individuals with SOD1 mutations enables direct comparison between the SOD1 mutant mouse model and a human system, providing a more

physiologically relevant context for studying the effects of SOD1 mutations. Inflammation is a hallmark of ALS, with microglia and astrocytes playing critical roles. While we aimed to investigate both cell types, a comparable dataset for iPSC-derived microglia was unavailable. Therefore, we focused on iPSC-derived astrocytes. We directly evaluated hiPSC-derived astrocytes from patients carrying mutations in SOD1[55], C9orf72[56], VCP[57], and FUS[58]. Data from all studies were processed using the same standardized pipeline and quality control metrics (Fig. 5l). Our analysis of DEGs revealed a consistent pattern across all four ALS-linked mutations (13 mutant lines and 14 control lines). Approximately ∽15% ($P_{Fisher} = 8.64 \times 10^{-16}$) of upregulated genes in at least one mutation to be ISGs, while the proportion of ISGs within the downregulated cluster was significantly lower (∽3%) (Fig. 5m). Further breakdown revealed 42 genes co-regulated by IFN-I and -II, while 30 genes were specifically responsive to IFN-II. No genes were identified to be regulated solely by IFN-I and -III (Fig. 5m). This enrichment of ISGs, particularly those driven by IFN-II, mirrored findings in sporadic spinal cord tissue.

To assess the conservation of these signatures between human and mouse models, we compared our hiPSC ALS dataset with mouse ALS astrocytes models[59]. This analysis identified 41 genes commonly upregulated and 83 genes commonly downregulated in both species. GO analysis of these shared DEGs revealed enrichment of genes associated with apoptosis and programmed cell death in the upregulated cluster (Fig. 5n). Meta-analysis of murine transcriptomic datasets longitudinally further validated this finding, demonstrating a strong correlation between the expression of IFN-I and IFN-II-induced ISGs and the upregulation of various cell death-related genes in G93A mice (median Pearson $R_{G93A} = 0.825$) (Supplementary Fig. 8). Specifically, we observed increased expression of genes associated with inflammasome (NLRC3, NLRC5, AIM2), proapoptotic factors (AIF1, HRK, BMF), extrinsic apoptosis (type I cell death, e.g. FAS, TNFSFs), autophagy (type II cell death, VAMP8, STX11, SNAP23, LAMP1), and necrosis (type III cell death, RIPK1, RIPK3, RIPK4) (Supplementary Fig. 8). Similar trends were noted for multiple caspase family genes, including initiator caspase CASP8, executioner caspase CASP6, and other caspases (CASP1, CASP4, CASP12). Concurrently, transcription factors known to directly or indirectly trigger cell death, such as JUN, JUNB, ATF3, NF-kBs, E2F8, FOXO1, and IRFs, were also upregulated in G93A mice (Supplementary Fig. 8). These findings collectively highlight the pivotal role of IFN-mediated programmed cell death in the pathogenesis of SOD1-associated ALS, providing a molecular basis for the improved muscle function and prolonged survival in our previous study upon IFNAR-blockade[14]. In agreement with this, pathways related to paralysis due to loss of supportive functions, such as neuromuscular and synapses development were enriched in the downregulated cluster (Fig. 5n). Notably, ISGs remained consistently present among the shared DEGs, with a higher proportion identified within the upregulated cluster (approximately 26%) compared to the downregulated cluster (approximately 7.4%) (Fig. 5n). We next examined the conservation of SAAS panel members across human samples. Of the five members, both CCL9 and TIMP1 were detected in sporadic ALS tissues and hiPSC-derived astrocytes. In summary, our findings in the iPSC-derived astrocytes model reinforce previous observations in murine and human spinal cord tissues. They collectively demonstrate a gain of inflammatory processes and a loss of supportive functions due to extensive cell death in both human and mouse ALS models. Importantly, this study strengthens the evidence for consistent presence of IFN-I, IFN-II and their associated ISGs in a physiologically relevant human ALS model system.

## SOD1 ALS mutation drive type II interferon production via STING and TBK1

To further elucidate the underlying mechanisms, we focused on ATF3, an ISG and SAAS member, ATF3 was persistently upregulated from P56 through P150 in SOD1-ALS model, leading us to hypothesize that it might modulate the heightened inflammatory responses, including IFN signaling. To investigate this, we utilized small-interfering RNA (siRNA) to inhibit ATF3 expression in the human microglia cell line HMC3. Two siRNAs targeting ATF3 (#1, #2) displayed significant knockdown efficiency and were selected for further analysis (Fig. 6a). Following siRNA-mediated ATF3 knockdown, cells were transfected with plasmids expressing ALS-causing SOD1 mutants and subsequently analyzed for gene expression. Notably, IFNB1, IFNG, and a IFN-II specific ISG CXCL9[60] expression increased significantly in ATF3 siRNA-treated cells compared to control siRNA-treated cells upon expression of G93A and G85R mutants (Fig. 6a). A similar increased was observed with the positive control, synthetic dsRNA mimic poly(I:C), which triggers IFN-I and -II responses (Fig. 6a). These results indicate that ATF3 depletion exacerbates the IFN-I and -II response, suggesting that ATF3 acts as a negative regulator of IFN-and other pro-inflammatory signaling pathways.

Given the previous implication of STING in ALS progression[14,15], we sought to investigate its potential role in IFN-II induction. For this purpose, we utilized both WT HEK293T cells (293T WT) and HEK293T cells stably expressing low levels of STING (293T STING). It is well-known that 293T WT cells deficient in STING component[61], and this pathway was restored upon reconstitution with low level of STING (Fig. 6b). IFN-II (IFN-γ) activated GAS element and ISRE luciferase reporter assays were performed in these HEK293T cells co-expressing either an empty vector or SOD1 mutants. Consistent with our previous report[14], all three SOD1 mutants (G93A, G85R and D90A) robustly induced IFN-I ISRE luciferase reporter activity in 293T STING but not in 293T WT cells (Fig. 6c), confirming the importance of STING pathway in SOD1 mutants-mediated IFN-I induction. Similarly, and in accordance with the positive controls using HT-DNA and recombinant IFN-γ, SOD1 mutant constructs were capable of activating IFN-γ-specific GAS luciferase reporters in a dose-dependent manner within 293T STING cells (Fig. 6c, middle and right); these effects, in turn, were significantly abrogated in 293T WT cells (Fig. 6c, left). Thus, the data suggest that STING is necessary for the induction of IFN-II responses by ALS-causing SOD1 mutants.

To further substantiate our findings, we employed a loss-of-function approach. siRNA targeting STING efficiently inhibit the expression of endogenous STING, while siRNA against MAVS served as a positive control for dsRNA sensing via the RIG-I-receptor pathway (Fig. 6d). We then measured the mRNA levels of IFNG, and the ISGs IRF7 and EIF2AK2 by RT-qPCR. The results showed a significant ($P < 0.001$) decrease in IFNG mRNA induction in G93A-expressing cells transfected with siSTING compared to those transfected with control siRNAs (Fig. 6e). A similar decrease was observed in mRNA levels of IRF7 and EIF2AK2, ISGs regulated by both IFN-I and -II[60] (Fig. 6e). In contrast, poly(I:C)-induced IFN-I and -II responses were unaffected by STING depletion, while siRNA targeting MAVS, a critical RIG-signaling adaptor, significantly abrogated the response (Fig. 6e). To ascertain the role of STING in SOD1 mutant-mediated IFN-II responses, we measured the expression of IFN-II specific ISGs via RT-qPCR[60]. Results consistently showed a significant reduction in the mRNA induction of CXCL9, IFITM1, GPR146 and TRIB3 in SOD1 mutant-expressing cells transfected with siSTING compared to control (Fig. 6f). We then extended this investigation by examining the role of TBK1, a downstream effector of STING. siRNA-mediated knockdown of TBK1 in human microglia cells significantly reduced the expression of IFN-II-specific ISGs (TRIB3 and GPR146) and IFNG mRNA (Fig. 6g). Next, we used fludarabine, a STAT1 inhibitor, to test the dependence of IFN-γ-specific ISGs induction on STAT1 homodimerization. Fludarabine treatment significantly ($P < 0.001$) abrogated both G93A and G85R-induced expression of TRIB3 and GPR146 (Fig. 6h). In comparison, the NF-κB inhibitor, SN50, had minimal effect on TRIB3 and GPR146 mRNA expression (Fig. 6h). Collectively, these results demonstrate that STING-TBK1 axis is essential for SOD1 mutant-induced IFN-II responses, highlighting the importance of the DNA sensing pathway in this ALS model.

In summary, our findings present a previously unreported mechanism whereby misfolded SOD1 triggers a complex inflammatory response. We demonstrate that misfolded SOD1 induces STING activation, leading to the production of both Type I (IFN-α/β) and Type II IFN (IFN-γ)
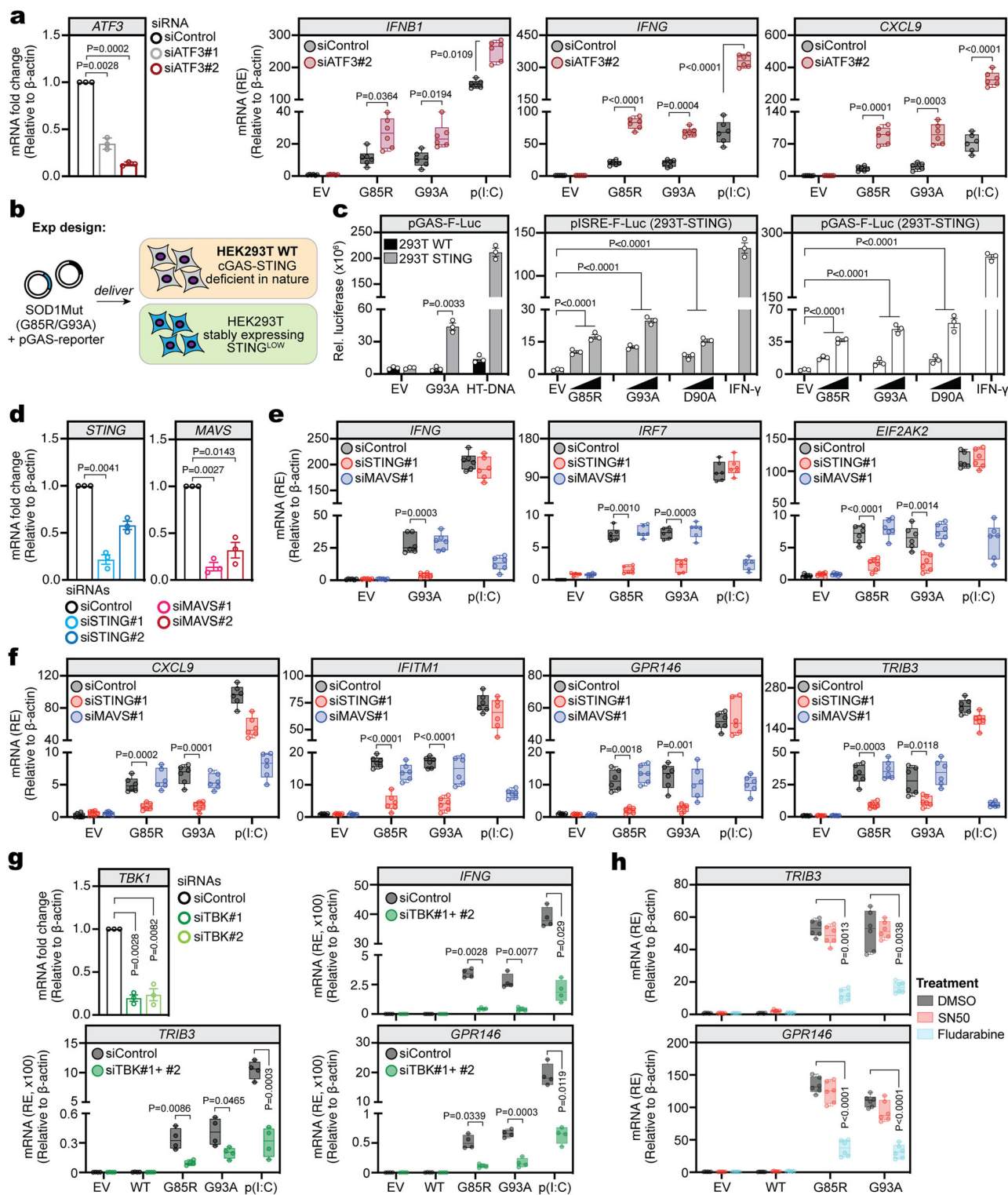
(Fig. 7). This, in turn, drives the expression of various ISGs, including both pro-inflammatory and anti-inflammatory mediators like ATF3 (Fig. 7). While this study focused primarily on SOD1-mediated ALS, we observed a consistent upregulation of IFN-I, IFN-II, and their associated ISGs in sporadic ALS patients as well. This suggests that the inflammatory pathways activated by misfolded SOD1, including the IFN axis and the downstream ISG response, may also play a role in sALS, where the underlying triggers of neuroinflammation are less well-defined. However,

further research is required to fully elucidate the specific contributions of these pathways to the pathogenesis of sALS. The presence of SAAS panel members and IFN-I and -II-associated ISGs throughout disease progression (pre-symptomatic, onset, and post-symptomatic) suggests their potential utility as biomarkers for improved diagnosis and monitoring of ALS, particularly in cases associated with misfolded SOD1. Our study also highlights a previously unreported role for STING in mediating IFN-γ-dependent responses in the context of misfolded protein pathologies.

Fig. 6 | STING-TBK1-dependent induction of Type II interferon responses in ALS model. a qPCR validation of the knockdown efficiency for ATF3 upon siRNA transfection in human microglia cells HMC3 ($n = 3$ per group). siRNA#2 were used. HMC3 cells were co-transfected with indicated siRNAs (50 nM) and expression vector (0.1 mg) for 48 h ($n = 6$ per group). Type I IFN gene (*IFNB1*), Type II IFN gene (*IFNG*), and IFNG-specific induced ISG (*CXCL9*) mRNA expressions were determined by RT-qPCR. Schematic diagram showing the experimental design. HEK293T WT and HEK293T expressing STING^{Low} cells were transfected either with pISRE-F-Luc or pGAS-F-Luc ($n = 3$ per group) (**b**). The transactivation of the reporter was assessed after 24 h (**c**). **d–f** Knockdown efficiency of STING and MAVS was measured ($n = 3$ per group) (**d**). HMC3 cells were co-transfected with siRNAs (50 nM) together either with SOD1 expression vector (0.1 mg) or poly(I:C) (0.1 mg) ($n = 6$ per group). *IFNG, IRF7, EIF2AK2* (**e**), *CXCL9, IFITM1, GPR146* and *TRIB3* (**f**)

mRNA was measured via RT-qPCR. **g** Knockdown efficiency of TBK1 was evaluated ($n = 3$ per group). HMC3 cells were co-transfected with siRNAs (50 nM) together either with SOD1 expression vector (0.1 mg) or poly(I:C) (0.1 mg). *IFNG, GPR146* and *TRIB3* mRNA was measured via RT-qPCR. **h** *TRIB3* and *GPR146* mRNA levels in HMC3-expressing indicated expression vectors after pre-treatment with [Vehicle: dimethyl sulfoxide (DMSO)], SN50 (10 mM, 24 h), or fludarabine (10 mM, 24 h) ($n = 6$ per group for each treatment). All expressions levels using qPCR were normalized against β-actin mRNA. Data represent the mean of at least three independent experiments with $n = 3$ biological replicates (mean ± SEM). Number of data-points = number of biological replicates. Unpaired student t-test with Welch's correction in **a, c** (*graph on left*)-**h** or one-way ANOVA with Bonferroni post-test in **c** (*graph at center and right*). *P*-values are shown within each graph, with baseline $p < 0.05$ considered statistically significant.
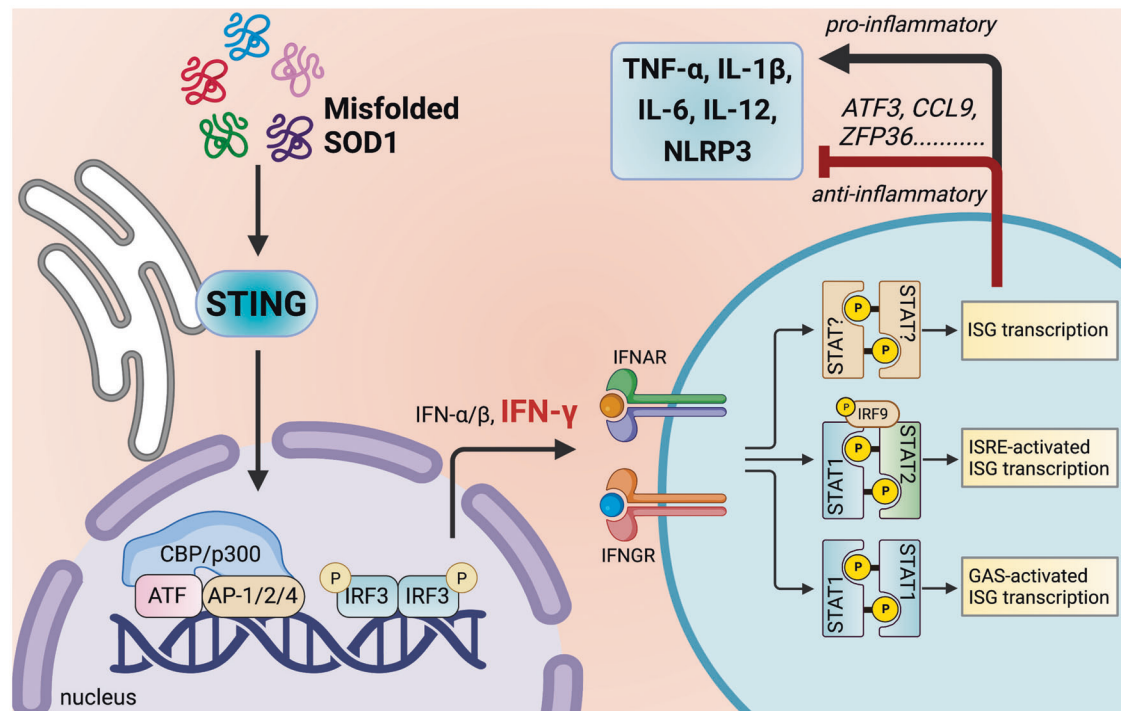

Fig. 7 | Summary of the main findings. Aberrant accumulation of misfolded SOD1 leads to increased expression of Type I and II IFN-inducible genes. Among these genes, a subset dependent on STAT1 activation, including *ATF3, CXCL9*, and *ZFP36*, show enhanced expression across different ALS stages. These genes primarily serve anti-inflammatory functions, acting as negative feedback loops to regulate the cytokine storm.

Discussion

ALS is characterized by a prolonged pre-symptomatic phase during which progressive motor neuron degeneration precedes clinical symptom onset[62]. This insidious progression complicates early therapeutic intervention, as irreversible neuronal loss often occurs before diagnosis. Inflammation is increasingly recognized as a critical factor in ALS pathogenesis, involving complex cascade of molecular and cellular events. To understand the temporal dynamics of these processes, we leveraged time-resolved expression data from murine models, which uniquely enable longitudinal tracking of early pre-symptomatic stages and disease progression—a critical advantage over human studies reliant on post-mortem tissues capturing only end-stage pathology.

Our prior work identified IFN-I and its associated ISGs as mediators of neuroinflammation in SOD1-associated ALS[14]. However, the static design of the study limited insights into IFN-I's temporal contribution to disease progression. It also remains unclear whether similar observations extend to human ALS. Here, we adopted a longitudinal approach to map dynamic gene expression changes throughout disease progression in mouse models. Analysis of DEGs revealed six distinct clusters denoting diverse dynamic trends, with Cluster 4 demonstrating a delayed, gradual increase in expression enriched for inflammatory pathways. This cluster was

significantly upregulated in G93A mice compared to WT controls. Integrated transcriptomic analysis across murine models, hiPSCs, and post-mortem spinal cords confirmed conserved activation of antiviral responses mediated by IFN-I. Unexpectedly, we also uncovered robust induction of IFN-II and IFN-II-inducible ISGs in both murine and human ALS samples, suggesting a cooperative role for both IFN families in disease mechanisms. While ISGs signatures were detectable in end-stage sporadic ALS tissues, clinical correlations between IFN-I and IFN-II levels and disease severity were inconclusive. This implies that ISGs expression alone may not reliably reflect disease activity. Variability in systemic IFN-I and IFN-II levels across patient cohorts, compounded by a lack of longitudinal autoantibody data, further complicates these associations. Nevertheless, our murine SOD1 model findings strongly implicate IFN pathways in ALS progression. In our longitudinal studies based on available genome-wide datasets, we consistently identified IFN-I and -II signatures in up to 40% of cases. This may explain the effectiveness of targeting IFN-I receptor (i.e. IFNAR) in ameliorating the disease in SOD1 murine model[14].

Our study also uncovered key species-specific differences between murine and human ALS. While broadly similar GO terms were enriched in both, a substantial fraction of murine DEGs lack conservation in human samples. For instance, *CXCL10*, a key chemoattractant for activated CD4$^+$

and CD8^{+} T-cells[63,64], was strongly upregulated in murine models, beginning as early as P95 (G86R) and P84 (G93A) and progressively increasing through end-stage disease. However, in human ALS, *CXCL10* was repressed. Despite this discrepancy, T-cell infiltration persists in human ALS tissues[65–67], consistent with observations in mouse models[14,68,69]. This suggests that other chemoattractants, such as *CCL2, CCL18*, and *CCL20*, which were strongly upregulated in human ALS, may compensate for the reduced *CXCL10* to facilitate T-cell recruitment. Furthermore, we identified a fundamental divergence in IFN responses between species. In the mouse ALS models, there was a predominant induction of IFN-I specific ISGs, which are typically associated with antiviral defense mechanisms, endogenous retro-elements activity, or viral-like processes. This association underpinned early ALS clinical trials, where researchers hypothesized a viral etiology based on clinical similarities with late post-polio syndrome, the presence of circulating viral-related immune antigens, and the detection of virus-like inclusions in ALS patients[70–74]. Consequently, recombinant IFN-α/β was tested as a potential treatment. However, these trials ultimately demonstrated that IFN-I administration neither ameliorated nor exacerbated disease progression[75–79], challenging the viral hypothesis of ALS. Our findings offer a potential explanation for this outcome: human sALS and SOD1-mutant iPSCs showed pronounced basal induction of IFN-II-specific ISGs, contrasting with the predominant IFN-I response in mice. This species-specific divergence in IFN signaling likely explains the inefficacy of IFN-I-targeted therapies in humans and underscores the need to prioritize IFN-II pathways in translational research. The basis for these differences remains unclear but likely stems from environmental or genetic factors that shape divergent immune landscapes. Our earlier GO analysis of human samples identified enriched adaptive immune pathways within the upregulated cluster, and subsequent ISGs analysis pinpointed IFN-γ (IFN-II) as a key driver. Consistent with IFN-γ's central role in adaptive immunity, its prominence in human ALS suggests a pronounced IFN-II-driven response, distinct from the disease trajectory in murine models. Such distinctions highlight the challenges of translating murine mechanistic insights into human therapeutics and reinforce the need to prioritize human-relevant models in preclinical studies.

Integrating population genetics with snRNA-seq data enabled us to assess cell-context-specific expression and ascribe functionality to ALS-associated variants. In G93A mutants, we observed a pronounced reduction in neuronal populations, consistent with the progressive motor neuron loss and muscle paralysis characteristics of ALS. Notably, while differentially expressed ISGs were detected across multiple cell types, vascular endothelial cells exhibited the most robust upregulation in terms of fold-change magnitude. This is finding particularly salient given the established link between ALS and endothelial dysfunction, which disproportionately impacts the blood-spinal cord barrier (BSCB). Murine models recapitulating ALS pathology demonstrate severe reductions in BSCB capillary length[80], while ALS patients exhibit structural compromise of BSCB endothelial cells[81], leading to barrier permeability, elevated immunoglobulin G levels, and immune cell infiltration into the CSF, motor cortex and spinal cord[82–84]. The pronounced ISGs induction we observed in endothelial cells suggests an active IFN-dependent inflammatory process localized to the vasculature. Such sustained ISGs activation may exacerbate BSCB dysfunction, promoting immune cell trafficking and amplifying neuroinflammatory cascades that drive disease progression. Notably, while astrocytes and microglia also differentially expressed ISGs, we detected no differential upregulation of *IFNB1, IFNA* or *IFNG* in any cell cluster within this snRNA-seq dataset. This contrasts with observations from bulk sequencing, raising critical questions about the cellular origins of IFN-I and IFN-II in this context. Potential sources include paracrine signaling from infiltrating immune cells or non-cell-autonomous IFN production that remains undetectable at the single-nucleus resolution employed here. Longitudinal snRNA-seq profiling with expanded cell numbers could help resolve these dynamics and clarify how spatiotemporal IFN signaling orchestrates neurovascular inflammation in ALS.

Finally, we investigated the mechanistic role of STING-TBK1 in IFN-II-inducible ISGs expression in SOD1 proteinopathy. Genetic depletion of STING and TBK1 significantly reduced IFN-II-specific ISGs induction in vitro, suggesting a relationship between STING-TBK1 dysregulation and misfolded SOD1-driven IFN-II response. This pathway may contribute to ALS severity by amplifying neuroinflammatory cascade. While our use of the INTERFEROME database has provided valuable insights into ISGs, establishing a definitive link between IFN-II signaling and disease progression will require further investigation. Future studies should consider crossbreeding IFNGR-knockout mice with SOD1-mutant murine models to directly test whether attenuating IFN-II signaling mitigates ALS-associated neurodegeneration.

In summary, our results collectively implicate sustained activation of both IFN-I and IFN-II pathways as potential biomarkers and drivers of ALS progression. The persistent upregulation of IFN-I/II and their downstream ISGs—particularly the robust co-induction observed across pathways—suggests a coordinated interplay that exacerbates neuroinflammation. These results align with growing evidence of IFN pathway dysregulation in ALS and other neurological disorders[85–87]. By mechanistic connecting STING-TBK1 signaling to IFN-II responses in SOD1-associated ALS, our study identifies previously unrecognized therapeutic targets. Elucidating the distinct contributions of IFN-I/II pathways and their effector ISGs could advance strategies for early diagnosis and precision therapies in ALS.

Methods
Public data collection, eligibility criteria, RNA-seq processing and quality control
We thoroughly searched public data repository including NCBI Gene Expression Omnibus (GEO; https://www.ncbi.nlm.nih.gov/geo/), NCBI Sequence Read Archive (SRA; https://www.ncbi.nlm.nih.gov/sra), and EBI ArrayExpress (https://www.ebi.ac.uk/arrayexpress/) for all eligible ALS expression datasets. Our search strategy incorporated keywords such as "SOD1", "ALS", "amyotrophic lateral sclerosis", "spinal cord", "time-points/course" and "RNA-seq". Sequencing datasets matching the same murine background strain (C57BL/6) and covering the data range from inception to 2022 were selected. The final search was conducted on December 31, 2022. For murine integrative analysis, we included a total of six datasets (GSE173524, GSE184484, GSE43879, GSE106803, GSE142654, and GSE106364) from distinct independent studies of ALS. Post-mortem spinal cord ALS RNA-seq samples were obtained from samples from the New York Genome Centre (NYGC) ALS Consortium cohort, with the GEO accession number of GSE137810. Although this large cohort datasets contained human samples derived from other regions of CNS, we specifically selected cervical spinal cord samples ($n = 275$ samples) and lumbar spinal cord samples ($n = 255$ samples) from both ALS patients and healthy controls for analysis. Diagnosis was determined by each contributing site. Additionally, we identified and integrated a total of six publicly available RNA-seq datasets for hiPSC-astrocytes related to VCP (GSE99843, GSE98288, GSE160133), SOD1 (GSE102902), C9orf72 (GSE142730), and FUS (GSE196219) into the meta-analyses.

GALAXY (https://usegalaxy.org/), a web-based computational platform, was employed for analyzing FASTQ files in this study. The FASTQ files obtained from the aforementioned samples' GEO accession numbers were uniformly processed in GALAXY[88,89] using the tool "Faster Download and Extract Reads in FASTQ" (v2.11.0). Quality control of the FASTQ files was performed using FastQC (v0.73). Poor-quality reads with a Phred quality score below 20 and reads shorter than 20 base pairs were eliminated using Cutadapt (v4.0), and ribosomal RNA removal were performed with SortMeRNA (v4.3.6)[90]. SortMeRNA was run with default parameters, utilizing the built-in rRNA reference databases derived from SILVA, Rfam and other resources. These databases provide a comprehensive collection of rRNA sequences for bacteria, archaea, and eukaryotes. On average, less than 5% of the reads in each sample were identified as rRNA and excluded from downstream analysis. Samples with rRNA content exceeding 10% were

excluded to ensure high-quality input for subsequent analyses. All analyzed samples met this criterion. We obtained Gene Transfer Format (GTF) files for the complete GRCh38/hg38 human reference genome and the complete mouse reference genome GRCm38/mm10 from the UCSC Genome Browser[91,92]. These files served as input for the splice-aware aligner, STAR v2.7.1, to align RNA-sequencing reads to both respective genomes. BAM-level quantification with Salmon was conducted. Gene expression in raw counts was measured using FeatureCounts (v2.0.1), counting only uniquely mapped reads. The integrated samples' RNA-sequencing data also underwent other extensive quality control analysis, including RSeQC, Qualimap, dupRadar, Preseq, SAMtools, and Picard (v2.22.3), with results collated using MultiQC (v1.8). Additionally, Gene Body Coverage (v2.6.4.3) were employed to analyze the uniformity of RNA-sequencing read coverage, while Read Distribution (v2.6.4.1) was used to analyze the distribution of mapped reads across different genomic features, including exon, intron, and intergenic regions. Infer Experiment (v2.6.4.1) determined the orientation of sequencing reads relative to the reference genome to identify the strandedness of the RNA-sequencing experiment.

We excluded datasets based on the following criteria: (i) not involving the spinal cord as the primary data source; (ii) lacking a time-course study design for murine species unless the sampling time-point(s) aligned with our study objective; (iii) absence of misfolded SOD1 as the primary ALS pathology in murine studies. For the human cohort, datasets from ALS-TDP, ALS/AD, ALS/FTLD groups were excluded, as well as spinal cord tissues from the thoracic segment, since this region is more associated with trunk stability. Additional exclusion criteria included: (iv) unadjusted batch effects between independent studies, such as different sequencing platforms between ALS and controls; (v) the use of long-read sequencing, and single-cell RNA-seq; and (vi) failure to meet specific sequencing quality thresholds, including a unique alignment rate below 90%, ribosomal bases of greater than 10%, a mismatch rate over 1%, duplication rate greater than 0.5%, intergenic bases below 10.5%, and ribosomal bases above 0.1%. All RNA-seq datasets included in our analysis passed these quality control thresholds, with unique alignment rates exceeding 90%. This ensured the selection of high-quality datasets for downstream analysis.

Differential expression analysis and GSEA

In this study, we conducted differential expression analysis using the *edgeR* software package (v3.40.0)[93] within R Studio (v4.2.2). Genes with a minimum counts per million (CPM) of 10 in at least one sample were retained for analysis. This filtering strategy removes genes likely exhibiting background noise rather than true biological expression, thereby focusing the analysis with meaningful contributions to biological processes. To accurately model the biological variability, we employed edgeR's negative binomial dispersion parameter for overall gene variability and the quasi-likelihood dispersion for gene-specific biological variability[93,94]. The negative binomial distribution was used to model the relationship between the variance and the mean of gene expression levels. We employed a generalized linear model to fit count data and separately estimate the dispersion parameter for each gene and across samples. This estimated dispersion was then used in likelihood calculations for accurately identifying differentially expressed genes. To minimize false discoveries, we applied the Benjamini-Hochberg false discovery rate (FDR) correction method[95]. Genes were considered differentially expressed genes between SOD1-mutant and wild-type samples if they met the criteria of FDR < 0.05 and a |Log2 fold change| ≥ 1. We performed gene set enrichment analysis (GSEA) to identify enriched functional categories among DEGs (FDR < 0.05). For our study, we used curated gene sets from the Molecular Signatures Database (MSigDB)[96]. A ranked gene list was generated based on log2-fold change values from the differential expression analysis. This ranked gene list was used as input for GSEA, which calculates an enrichment score (ES) for each gene set, reflecting the degree to which genes in a particular set are overrepresented at the top or bottom of the ranked gene list. The ES is then normalized to the size of the gene set, yielding a normalized enrichment score (NES). Further permutation testing was performed where sample labels were randomly shuffled multiple times,

and the ES was recalculated for each permutation. This generates a null distribution of NES values. Gene sets with an FDR < 0.05 were considered significantly enriched. To define the background gene set for GSEA, we included only those genes that had detectable expression in the tissue of interest, specifically genes with a CPM of at least 10 in at least one sample. This ensures that the background set is biologically relevant and reflects the genes actively expressed in the studied tissue, rather than including all genes in the genome. In parallel, we conducted overrepresentation analysis to test for enrichment of Gene Ontology terms and the Kyoto Encyclopedia of Genes and Genomes pathways among up- and downregulated genes (FDR < 0.05, |Log2 fold change| ≥ 1). These analyses were conducted using the clusterProfiler package (v4.7.0) in R-studio, with functional terms considered significant at FDR < 0.05.

Differential expression results for post-mortem spinal cord ALS were calculated by comparing ALS versus control samples. In brief, a data frame with sample IDs and columns for age, sex, batch, library preparation methods, and condition was created. A DGEList object was then created in *edgeR* using raw gene expression counts and the covariate data frame. Lowly expressed genes were filtered out using a criterion of CPM ≥10 in at least one sample. Next, we estimated normalization factors using *calcNormFactors* and then estimated the dispersion parameter using edgeR's *estimateDisp*, incorporating the design matrix formula: ~ *batch + library_prep + age + sex + condition*. The model was then fitted using *glmQLFit*, and quasi-likelihood F-tests were conducted using *glmQLFTest* to identify DEGs[97]. A results table with log2 fold changes, p-values, and FDR-adjusted p-values (FDR < 0.05) was extracted using *topTags* for downstream analysis.

Analysis of snRNA-seq data

Quality control and cell selection. Quality control and cell selection was performed using the Seurat R package (v5.0.1) to analyzed the gene-count matrix for GSE173524. This analysis included data scaling, transformation, clustering, dimensionality reduction, and visualization. As an initial reference, principal component analysis was performed on the variable genes, and t-SNE was run on the top 10 principal components using the Multicore-TSNE package. Cell quality was assessed based on the following metrics: (i) the number of genes for which at least one read was mapped; (ii) the total number of counts; and (iii) the percentage of reads mapped to mitochondrial genes, often used to estimate endogenous RNA levels and assess cell quality. Cells with a high mitochondrial-to-endogenous RNA ratio were removed, as this suggests potential RNA degradation due to cell death or stress. Then, a unique molecular identifier (UMI) of 200 was applied for cell selection. This threshold was established based on a previous pilot study[98] demonstrating that the default 10x Genomics cell-detection method failed to capture a significant portion of the microglia population. Histogram analysis of cell density as a function of UMI values confirmed 200 UMIs as the lower threshold for cell filtering[98]. Based on these observations and subsequent scatter-plot analyses, cells with fewer than 200 detected genes and those with a high mitochondrial gene counts ratio (greater than 10%) were excluded. Outlier cells, identified based on mitochondrial ratios using *k*-means clustering (*k* = 2), were also removed. These filtering steps yielded 14,662 high quality nuclei for further analyses.

Cell type annotation and clustering. Cell type annotation and clustering were performed using a two-step process. First, each pre-cluster was assigned a cell type label based on statistical enrichment of marker genes and manual evaluation of known marker gene expression. Enrichment was assessed using the hypergeometric distribution (Fisher's exact test) with FDR correction. Broad cell-type clusters were then defined by grouping pre-clusters with the same cell type label. To identify sub-clusters within each broad cell type, a second round of clustering was performed independently on vascular cells and neurons. This resulted in three distinct cell subsets. The final annotation was harmonized with the Azimuth reference dataset using Seurat[48]. For each of the ten identified clusters, the percentage of cells mapped to each Azimuth annotation was calculated to assess concordance.

Single-cell differential gene expression. Single-cell differential gene expression analysis was performed using the *FindMarkers* function in Seurat with Benjamini-Hochberg multiple testing correction. Genes expressed (UMI count >0) in more than 10% of cells per cell type were included in the analysis. Differentially expressed genes were defined as those with an adjusted *p*-value < 0.05 and an average fold change ≥0.5 were considered. Gene Ontology enrichment analyses were then conducted using gProfileR, with *p*-value ranked gene lists as input.

Correlation analysis. Spearman's rank correlations coefficients were calculated with the function rcorr in the hmisc R package (v5.1-3). The correlation coefficients were visualized using the corrplot function, with positive correlations displayed in red and negative correlations in green.

Cell lines and culture condition
Both HEK293T (#CRL-3216) and HMC3 cell lines (#CRL-3304) were obtained from American Type Culture Collection (ATCC). Cells were grown in Dulbecco's modified Eagle medium containing 10% fetal bovine serum (Gibco) and 1% penicillin-streptomycin-amphotericin B (SolarBio) and cryopreserved in Cell Reservoir One solution (Nacalai Tesque) as low-passage stocks. All cell lines were regularly tested for mycoplasma contamination using mycoplasma detection kit (InvivoGen). All cell lines tested mycoplasma negative.

RNA extraction and RT-qPCR
Gene expression analysis shown in Supplementary Fig. 4 utilized previously extracted and purified RNA samples[14]. The transcript levels of indicated genes was measured by reverse transcription quantitative PCR (RT-qPCR) as previously described[99]. In brief, total RNA was extracted with TriQuick reagent (SolarBio) according to the manufacturer's instructions. We then treated 100 ng of total RNA with recombinant DNase I (10 units/uL; NEB) at 37°C for one hour and purified the samples using phenol-chloroform extraction. cDNA was synthesized from 100 ng of purified RNA using SensiFAST cDNA synthesis kit (Bioline, Meridian BioScience). Subsequently, qPCR analysis was performed using SensiFAST SYBR (Bioline, Meridian Bioscience) and specific probes (Supplementary Table 1). Expression levels were normalized to the housekeeping genes *ACTB* and calculated using the $2^{-\Delta\Delta Ct}$ method.

RNA interference and plasmid expression
For knockdown experiments, we transfected cells with siRNA (Stealth RNAi, ThermoFisher Scientific) using the Lipofectamine RNAiMax (ThermoFisher Scientific) in accordance with the manufacturer's instructions. Knockdown efficiency was confirmed by qRT-PCR. Primer sequences are listed in Supplementary Table 1. Expression vectors are transfected using JetPrime (PolyPlus, Sartorius). Co-transfection of siRNAs and plasmids were performed using Lipofectamine2000 as per the manufacturer's instructions.

Luciferase reporter gene assay
We co-transfected HEK293T cells with a mixture of the luciferase reporter plasmids, the pRL-TK-Renilla-luciferase control plasmid, and either SOD1 wild type or mutant plasmids. 24–36 h later, we measured luciferase activities using the Dual Luciferase Reporter Assay System (Promega) following the manufacturer's instructions. Data are normalized for transfection efficiency by dividing *Firefly* luciferase activity with the activity of *Renilla* luciferase.

Enzyme-linked immunosorbent assay (ELISA)
Serum IFN-γ levels were quantified in mouse blood samples (obtained in our previous study[14]) using a commercial kit (BioLegend) according to the manufacturer's instruction. Briefly, 96-well high-binding polystyrene plates (BIO-LOGIX) were coated overnight at 4 °C with 4 μg/mL of mouse IFN-γ capture antibody in coating buffer. After washing (4x, wash buffer provided with the kit), plates were blocked for one hour at room temperature with *Assay Diluent*.

Immediately after blocking, serially diluted serum samples (initial dilution of 1:200 in *Assay Diluent*) and standards (starting concentration 10 μg/mL) were added to the wells and incubated for two hours at room temperature. Following another wash step (4x), the *Detection Antibody* was added and incubated for one hour at room temperature. Plates were then washed again, and avidin-conjugated to HRP (1:1000 dilution in blocking buffer) was added for 30 min at room temperature. Absorbance was measured and background-corrected using a standard curve generated in Excel spreadsheet and Prism (GraphPad, v8).

Statistics and reproducibility
We performed all statistical analyses using either R-Studio or Prism (GraphPad Software, version 8). The figure legends specify the number of replicates and the type of tests conducted. The numbers of biological replicates were chosen based on the nature of the experiments and published papers describing similar experiments. To compare two groups, we used a two-tailed unpaired Student's *t*-test, while for more than two groups, we employed one- or two-way ANOVA with the least significant difference *t*-test. Fisher's exact test was performed on 2 × 2 contingency to determine if the proportion of ISGs among the G93A mutant was significant. Data in graphs are presented as mean±S.E.M. Data distribution was assumed to be normal but this was not formally tested. The study sizes were not pre-determined using statistical methods but were based on similar experiments previously published. The experiments were not randomized and investigators were not blinded to allocation during experiments. Heatmaps, and volcano plots were generated using R-software.

Reporting summary
Further information on research design is available in the Nature Portfolio Reporting Summary linked to this article.

Data availability
All bulk and single-nucleus RNA-seq data supporting the findings of this study are publicly available through the Gene Expression Omnibus (GEO) under the accession numbers provided in the Methods section. Additional experimental data are also provided in the Supplementary Data 1, and on Figshare (https://doi.org/10.6084/m9.figshare.28296215).

Code availability
Analysis code used to generate figures in Fig. 1c for this paper are available at https://github.com/ngchenseng/STING-IFN-II-induction-in-ALS/.

References
1. van Es, M. A. et al. Amyotrophic lateral sclerosis. *Lancet* **390**, 2084–2098 (2017).
2. Barberio, J., Lally, C., Kupelian, V., Hardiman, O. & Flanders, W. D. Estimated Familial Amyotrophic Lateral Sclerosis Proportion: A Literature Review and Meta-analysis. *Neurol. Genet.* **9**, e200109 (2023).
3. Renton, A. E. et al. A hexanucleotide repeat expansion in C9ORF72 is the cause of chromosome 9p21-linked ALS-FTD. *Neuron* **72**, 257–268 (2011).
4. Rosen, D. R. et al. Mutations in Cu/Zn superoxide dismutase gene are associated with familial amyotrophic lateral sclerosis. *Nature* **362**, 59–62 (1993).
5. Kwiatkowski, T. J. et al. Mutations in the FUS/TLS gene on chromosome 16 cause familial amyotrophic lateral sclerosis. *Science* **323**, 1205–1208 (2009).
6. Kabashi, E. et al. TARDBP mutations in individuals with sporadic and familial amyotrophic lateral sclerosis. *Nat. Genet.* **40**, 572–574 (2008).
7. Evans, M. C., Couch, Y., Sibson, N. & Turner, M. R. Inflammation and neurovascular changes in amyotrophic lateral sclerosis. *Mol. Cell. Neurosci.* **53**, 34–41 (2013).

8. Liu, J. & Wang, F. Role of neuroinflammation in amyotrophic lateral sclerosis: cellular mechanisms and therapeutic implications. *Front. Immunol.* **8**, 1005 (2017).

9. Phatnani, H. & Maniatis, T. Astrocytes in neurodegenerative disease. *Cold Spring Harb. Perspect. Biol.* **7**, a018812 (2015).

10. Meyer, K. et al. Direct conversion of patient fibroblasts demonstrates non-cell autonomous toxicity of astrocytes to motor neurons in familial and sporadic ALS. *Proc. Natl. Acad. Sci. USA* **111**, 829–832 (2014).

11. Verkhratsky, A. et al. Astrocytes in human central nervous system diseases: a frontier for new therapies. *Signal Transduct. Target. Ther.* **8**, 396 (2023).

12. Papadeas, S. T., Kraig, S. E., O'Banion, C., Lepore, A. C. & Maragakis, N. J. Astrocytes carrying the superoxide dismutase 1 (SOD1G93A) mutation induce wild-type motor neuron degeneration in vivo. *Proc. Natl. Acad. Sci. USA* **108**, 17803–17808 (2011).

13. Murdock, B. J., Bender, D. E., Segal, B. M. & Feldman, E. L. The dual roles of immunity in ALS: injury overrides protection. *Neurobiol. Dis.* **77**, 1–12 (2015).

14. Tan, H. Y. et al. cGAS and DDX41-STING mediated intrinsic immunity spreads intercellularly to promote neuroinflammation in SOD1 ALS model. *iScience* **25**, 104404 (2022).

15. Yu, C.-H. et al. TDP-43 Triggers Mitochondrial DNA Release via mPTP to Activate cGAS/STING in ALS. *Cell* **183**, 636–649.e18 (2020).

16. McCauley, M. E. et al. C9orf72 in myeloid cells suppresses STING-induced inflammation. *Nature* **585**, 96–101 (2020).

17. Marques, C. et al. Neuronal STING activation in amyotrophic lateral sclerosis and frontotemporal dementia. *Acta Neuropathol.* **147**, 56 (2024).

18. Maniatis, S. et al. Spatiotemporal dynamics of molecular pathology in amyotrophic lateral sclerosis. *Science* **364**, 89–93 (2019).

19. Phatnani, H. P. et al. Intricate interplay between astrocytes and motor neurons in ALS. *Proc. Natl. Acad. Sci. USA* **110**, E756–E765 (2013).

20. Krasemann, S. et al. The TREM2-APOE pathway drives the transcriptional phenotype of dysfunctional microglia in neurodegenerative diseases. *Immunity* **47**, 566–581.e9 (2017).

21. Deczkowska, A. et al. Disease-Associated Microglia: A Universal Immune Sensor of Neurodegeneration. *Cell* **173**, 1073–1081 (2018).

22. Lee, S.-H. et al. TREM2-independent oligodendrocyte, astrocyte, and T cell responses to tau and amyloid pathology in mouse models of Alzheimer disease. *Cell Rep.* **37**, 110158 (2021).

23. Huang, Z. et al. Circadian rhythm dysfunction accelerates disease progression in a mouse model with amyotrophic lateral sclerosis. *Front. Neurol.* **9**, 218 (2018).

24. Leng, Y., Musiek, E. S., Hu, K., Cappuccio, F. P. & Yaffe, K. Association between circadian rhythms and neurodegenerative diseases. *Lancet Neurol.* **18**, 307–318 (2019).

25. Wong, P. C. et al. An adverse property of a familial ALS-linked SOD1 mutation causes motor neuron disease characterized by vacuolar degeneration of mitochondria. *Neuron* **14**, 1105–1116 (1995).

26. Gurney, M. E. et al. Motor neuron degeneration in mice that express a human Cu,Zn superoxide dismutase mutation. *Science* **264**, 1772–1775 (1994).

27. De Vos, K. J. & Hafezparast, M. Neurobiology of axonal transport defects in motor neuron diseases: Opportunities for translational research? *Neurobiol. Dis.* **105**, 283–299 (2017).

28. Brites, D. & Vaz, A. R. Microglia centered pathogenesis in ALS: insights in cell interconnectivity. *Front. Cell Neurosci.* **8**, 117 (2014).

29. Singh, T. et al. Neuronal mitochondrial dysfunction in sporadic amyotrophic lateral sclerosis is developmentally regulated. *Sci. Rep.* **11**, 18916 (2021).

30. Lazear, H. M., Schoggins, J. W. & Diamond, M. S. Shared and distinct functions of type I and type III interferons. *Immunity* **50**, 907–923 (2019).

31. Samarajiwa, S. A., Forster, S., Auchettl, K. & Hertzog, P. J. INTERFEROME: the database of interferon regulated genes. *Nucleic Acids Res.* **37**, D852–D857 (2009).

32. Rusinova, I. et al. Interferome v2.0: an updated database of annotated interferon-regulated genes. *Nucleic Acids Res.* **41**, D1040–D1046 (2013).

33. Ripps, M. E., Huntley, G. W., Hof, P. R., Morrison, J. H. & Gordon, J. W. Transgenic mice expressing an altered murine superoxide dismutase gene provide an animal model of amyotrophic lateral sclerosis. *Proc. Natl. Acad. Sci. USA* **92**, 689–693 (1995).

34. Chen, K., Xu, M., Lu, F. & He, Y. Development of Matrix Metalloproteinases-Mediated Extracellular Matrix Remodeling in Regenerative Medicine: A Mini Review. *Tissue Eng. Regen. Med.* **20**, 661–670 (2023).

35. Trentini, A. et al. TIMP-1 resistant matrix metalloproteinase-9 is the predominant serum active isoform associated with MRI activity in patients with multiple sclerosis. *Mult. Scler.* **21**, 1121–1130 (2015).

36. Avolio, C. et al. Serum MMP-9/TIMP-1 and MMP-2/TIMP-2 ratios in multiple sclerosis: relationships with different magnetic resonance imaging measures of disease activity during IFN-beta-1a treatment. *Mult. Scler.* **11**, 441–446 (2005).

37. Lindberg, R. L. et al. The expression profile of matrix metalloproteinases (MMPs) and their inhibitors (TIMPs) in lesions and normal appearing white matter of multiple sclerosis. *Brain* **124**, 1743–1753 (2001).

38. Skuljec, J. et al. Matrix metalloproteinases and their tissue inhibitors in cuprizone-induced demyelination and remyelination of brain white and gray matter. *J. Neuropathol. Exp. Neurol.* **70**, 758–769 (2011).

39. Fernández-Beltrán, L. C. et al. A Transcriptomic Meta-Analysis Shows Lipid Metabolism Dysregulation as an Early Pathological Mechanism in the Spinal Cord of SOD1 Mice. *Int. J. Mol. Sci.* **22**, 9553 (2021).

40. Crow, M. K., Olferiev, M. & Kirou, K. A. Type I interferons in autoimmune disease. *Annu. Rev. Pathol.* **14**, 369–393 (2019).

41. Muskardin, T. L. W. & Niewold, T. B. Type I interferon in rheumatic diseases. *Nat. Rev. Rheumatol.* **14**, 214–228 (2018).

42. Park, A. & Iwasaki, A. Type I and Type III Interferons - Induction, Signaling, Evasion, and Application to Combat COVID-19. *Cell Host Microbe* **27**, 870–878 (2020).

43. Pujato, M., Kieken, F., Skiles, A. A., Tapinos, N. & Fiser, A. Prediction of DNA binding motifs from 3D models of transcription factors; identifying TLX3 regulated genes. *Nucleic Acids Res.* **42**, 13500–13512 (2014).

44. Thompson, M. R., Xu, D. & Williams, B. R. G. ATF3 transcription factor and its emerging roles in immunity and cancer. *J. Mol. Med.* **87**, 1053–1060 (2009).

45. Ko, C.-Y., Chang, W.-C. & Wang, J.-M. Biological roles of CCAAT/Enhancer-binding protein delta during inflammation. *J. Biomed. Sci.* **22**, 6 (2015).

46. Zhou, J. et al. Anti-inflammatory Activity of MTL-CEBPA, a Small Activating RNA Drug, in LPS-Stimulated Monocytes and Humanized Mice. *Mol. Ther.* **27**, 999–1016 (2019).

47. MacLean, M., López-Díez, R., Vasquez, C., Gugger, P. F. & Schmidt, A. M. Neuronal-glial communication perturbations in murine SOD1G93A spinal cord. *Commun. Biol.* **5**, 177 (2022).

48. Hao, Y. et al. Integrated analysis of multimodal single-cell data. *Cell* **184**, 3573–3587 (2021).

49. Kurowarabe, K., Endo, M., Kobayashi, D. & Hayasaka, H. CXCL12-stimulated lymphocytes produce secondary stimulants that affect the surrounding cell chemotaxis. *Biochem. Biophys. Rep.* **28**, 101128 (2021).

50. NCBI Resource Coordinators. Database resources of the National Center for Biotechnology Information. *Nucleic Acids Res.* **41**, D8–D20 (2013).

51. Pangou, E. & Sumara, I. The multifaceted regulation of mitochondrial dynamics during mitosis. *Front. Cell Dev. Biol.* **9**, 767221 (2021).

52. Mayya, C. et al. The roles of dynein and myosin VI motor proteins in endocytosis. *J. Cell Sci.* **135**, jcs259387 (2022).

53. Dwivedi, D. & Sharma, M. Multiple roles, multiple adaptors: dynein during cell cycle. *Adv. Exp. Med. Biol.* **1112**, 13–30 (2018).

54. Raaijmakers, J. A. & Medema, R. H. Function and regulation of dynein in mitotic chromosome segregation. *Chromosoma* **123**, 407–422 (2014).

55. Tyzack, G. E. et al. A neuroprotective astrocyte state is induced by neuronal signal EphB1 but fails in ALS models. *Nat. Commun.* **8**, 1164 (2017).

56. Birger, A. et al. Human iPSC-derived astrocytes from ALS patients with mutated C9ORF72 show increased oxidative stress and neurotoxicity. *EBioMedicine* **50**, 274–289 (2019).

57. Hall, C. E. et al. Progressive Motor Neuron Pathology and the Role of Astrocytes in a Human Stem Cell Model of VCP-Related ALS. *Cell Rep.* **19**, 1739–1749 (2017).

58. Stoklund Dittlau, K. et al. FUS-ALS hiPSC-derived astrocytes impair human motor units through both gain-of-toxicity and loss-of-support mechanisms. *Mol. Neurodegener.* **18**, 5 (2023).

59. Ziff, O. J. et al. Reactive astrocytes in ALS display diminished intron retention. *Nucleic Acids Res.* **49**, 3168–3184 (2021).

60. Liu, S.-Y., Sanchez, D. J., Aliyari, R., Lu, S. & Cheng, G. Systematic identification of type I and type II interferon-induced antiviral factors. *Proc. Natl. Acad. Sci. USA* **109**, 4239–4244 (2012).

61. Sun, L., Wu, J., Du, F., Chen, X. & Chen, Z. J. Cyclic GMP-AMP synthase is a cytosolic DNA sensor that activates the type I interferon pathway. *Science* **339**, 786–791 (2013).

62. Eisen, A., Kiernan, M., Mitsumoto, H. & Swash, M. Amyotrophic lateral sclerosis: a long preclinical period? *J. Neurol. Neurosurg. Psychiatry* **85**, 1232–1238 (2014).

63. Peperzak, V. et al. CD8+ T cells produce the chemokine CXCL10 in response to CD27/CD70 costimulation to promote generation of the CD8+ effector T cell pool. *J. Immunol.* **191**, 3025–3036 (2013).

64. Karin, N. CXCR3 ligands in cancer and autoimmunity, chemoattraction of effector T cells, and beyond. *Front. Immunol.* **11**, 976 (2020).

65. Engelhardt, J. I., Tajti, J. & Appel, S. H. Lymphocytic infiltrates in the spinal cord in amyotrophic lateral sclerosis. *Arch. Neurol.* **50**, 30–36 (1993).

66. Fiala, M. et al. IL-17A is increased in the serum and in spinal cord CD8 and mast cells of ALS patients. *J. Neuroinflam.* **7**, 76 (2010).

67. Kawamata, T., Akiyama, H., Yamada, T. & McGeer, P. L. Immunologic reactions in amyotrophic lateral sclerosis brain and spinal cord tissue. *Am. J. Pathol.* **140**, 691–707 (1992).

68. Chiu, I. M. et al. T lymphocytes potentiate endogenous neuroprotective inflammation in a mouse model of ALS. *Proc. Natl. Acad. Sci. USA* **105**, 17913–17918 (2008).

69. Beers, D. R., Henkel, J. S., Zhao, W., Wang, J. & Appel, S. H. CD4+ T cells support glial neuroprotection, slow disease progression, and modify glial morphology in an animal model of inherited ALS. *Proc. Natl. Acad. Sci. USA* **105**, 15558–15563 (2008).

70. Okamoto, K., Mizuno, Y. & Fujita, Y. Bunina bodies in amyotrophic lateral sclerosis. *Neuropathology* **28**, 109–115 (2008).

71. Fallis, R. J. & Weiner, L. P. Further studies in search of a virus in amyotrophic lateral sclerosis. *Adv. Neurol.* **36**, 355–361 (1982).

72. Martyn, C. N., Barker, D. J. & Osmond, C. Motoneuron disease and past poliomyelitis in England and Wales. *Lancet* **1**, 1319–1322 (1988).

73. Westarp, M. E. et al. Antiretroviral therapy in sporadic adult amyotrophic lateral sclerosis. *Neuroreport* **4**, 819–822 (1993).

74. Bartfeld, H. et al. Enteroviral-related antigen in circulating immune complexes of amyotrophic lateral sclerosis patients. *Intervirology* **30**, 202–212 (1989).

75. Rissanen, A., Palo, J., Myllylä, G. & Cantell, K. Interferon therapy for ALS. *Ann. Neurol.* **7**, 392 (1980).

76. Beghi, E. et al. A randomized controlled trial of recombinant interferon beta-1a in ALS. Italian Amyotrophic Lateral Sclerosis Study Group. *Neurology* **54**, 469–474 (2000).

77. Mora, J. S. et al. Intrathecal administration of natural human interferon alpha in amyotrophic lateral sclerosis. *Neurology* **36**, 1137–1140 (1986).

78. Dalakas, M. C., Aksamit, A. J., Madden, D. L. & Sever, J. L. Administration of recombinant human leukocyte alpha 2-interferon in patients with amyotrophic lateral sclerosis. *Arch. Neurol.* **43**, 933–935 (1986).

79. Westarp, M. E. et al. Dermal, serological and CSF changes in amyotrophic lateral sclerosis with and without intrathecal interferon beta treatment. *Int J. Clin. Pharm. Ther. Toxicol.* **30**, 81–93 (1992).

80. Winkler, E. A. et al. Blood-spinal cord barrier breakdown and pericyte reductions in amyotrophic lateral sclerosis. *Acta Neuropathol.* **125**, 111–120 (2013).

81. Garbuzova-Davis, S. et al. Evidence of compromised blood-spinal cord barrier in early and late symptomatic SOD1 mice modeling ALS. *PLoS One* **2**, e1205 (2007).

82. Engelhardt, J. I. & Appel, S. H. IgG reactivity in the spinal cord and motor cortex in amyotrophic lateral sclerosis. *Arch. Neurol.* **47**, 1210–1216 (1990).

83. Donnenfeld, H., Kascsak, R. J. & Bartfeld, H. Deposits of IgG and C3 in the spinal cord and motor cortex of ALS patients. *J. Neuroimmunol.* **6**, 51–57 (1984).

84. Leonardi, A., Abbruzzese, G., Arata, L., Cocito, L. & Vische, M. Cerebrospinal fluid (CSF) findings in amyotrophic lateral sclerosis. *J. Neurol.* **231**, 75–78 (1984).

85. Main, B. S. et al. Type-1 interferons contribute to the neuroinflammatory response and disease progression of the MPTP mouse model of Parkinson's disease. *Glia* **64**, 1590–1604 (2016).

86. Quan, P. et al. Single cell analysis reveals the roles and regulatory mechanisms of type-I interferons in Parkinson's disease. *Cell Commun. Signal.* **22**, 212 (2024).

87. Roy, E. R. et al. Type I interferon response drives neuroinflammation and synapse loss in Alzheimer disease. *J. Clin. Invest.* **130**, 1912–1930 (2020).

88. Afgan, E. et al. The Galaxy platform for accessible, reproducible and collaborative biomedical analyses: 2018 update. *Nucleic Acids Res.* **46**, W537–W544 (2018).

89. Galaxy Community. The Galaxy platform for accessible, reproducible and collaborative biomedical analyses: 2022 update. *Nucleic Acids Res.* **50**, W345–W351 (2022).

90. Kopylova, E., Noé, L. & Touzet, H. SortMeRNA: fast and accurate filtering of ribosomal RNAs in metatranscriptomic data. *Bioinformatics* **28**, 3211–3217 (2012).

91. Lee, B. T. et al. The UCSC Genome Browser database: 2022 update. *Nucleic Acids Res* **50**, D1115–D1122 (2022).

92. Nassar, L. R. et al. The UCSC Genome Browser database: 2023 update. *Nucleic Acids Res.* **51**, D1188–D1195 (2023).

93. Robinson, M. D., McCarthy, D. J. & Smyth, G. K. edgeR: a Bioconductor package for differential expression analysis of digital gene expression data. *Bioinformatics* **26**, 139–140 (2010).

94. Chen, Y., Lun, A. T. L. & Smyth, G. K. From reads to genes to pathways: differential expression analysis of RNA-Seq experiments using Rsubread and the edgeR quasi-likelihood pipeline. [version 2; peer review: 5 approved]. *F1000Res* **5**, 1438 (2016).

95. Benjamini, Y. & Hochberg, Y. Controlling the false discovery rate: a practical and powerful approach to multiple testing. *J. R. Stat. Soc.: Ser. B (Methodol.)* **57**, 289–300 (1995).

96. Liberzon, A. et al. The Molecular Signatures Database (MSigDB) hallmark gene set collection. *Cell Syst.* **1**, 417–425 (2015).

97. Lund, S. P., Nettleton, D., McCarthy, D. J. & Smyth, G. K. Detecting differential expression in RNA-sequence data using quasi-likelihood with shrunken dispersion estimates. *Stat. Appl. Genet. Mol. Biol.* **11**, 1–42 (2012).

98. Mathys, H. et al. Single-cell transcriptomic analysis of Alzheimer's disease. *Nature* **570**, 332–337 (2019).

99. Ng, C. S., Kasumba, D. M., Fujita, T. & Luo, H. Spatio-temporal characterization of the antiviral activity of the XRN1-DCP1/2 aggregation against cytoplasmic RNA viruses to prevent cell death. *Cell Death Differ.* **27**, 2363–2382 (2020).

100. Herskovits, A. Z. et al. SIRT1 deacetylase in aging-induced neuromuscular degeneration and amyotrophic lateral sclerosis. *Aging Cell* **17**, e12839 (2018).

101. Fernández-Beltrán, L. C. et al. Leptin haploinsufficiency exerts sex-dependent partial protection in SOD1G93A mice by reducing inflammatory pathways in the adipose tissue. *Sci. Rep.* **14**, 2671 (2024).

102. Luisier, R. et al. Intron retention and nuclear loss of SFPQ are molecular hallmarks of ALS. *Nat. Commun.* **9**, 2010 (2018).

Author contributions

J.Y.H. and C.S.N. conceived and designed the research. J.Y.H. and H.L. performed computational analyses of all functional genomic and single-nuclear transcriptomic data. Y.S.L., and H.L. performed the experiments and data analysis, with supervisorial input from C.S.N. C.S.N. also performed some experiments and assisted with the computational analysis. All authors contributed to writing the paper and making the figures.

Competing interests

The authors declare no competing interests.

Additional information

Supplementary information The online version contains supplementary material available at https://doi.org/10.1038/s42003-025-07790-w.

Correspondence and requests for materials should be addressed to Chen Seng Ng.

Peer review information *Communications Biology* thanks David Mack and the other, anonymous, reviewer(s) for their contribution to the peer review of this work. Primary Handling Editors: Eliana Scemes and Dario Ummarino.

Reprints and permissions information is available at http://www.nature.com/reprints

Publisher's note Springer Nature remains neutral with regard to jurisdictional claims in published maps and institutional affiliations.